Examining the d(n,nd) and d(n,np)n Reactions for Evidence of a Three-Nucleon Interaction

By

Christopher M. Wells

A thesis submitted in partial fulfillment of the requirements for the degree of

Bachelor of Science

Houghton College

May 2005

Signature of Author…………………………………………………………………………..............................
Department of Physics

…………………………………………………………………………………………..................................
Dr. Mark Yuly
Professor of Physics
Research Supervisor

…………………………………………………………………………………………..................................
Dr. Ronald Rohe
Associate Professor of Physics

Examining the d(n,nd) and d(n,np)n Reactions For Evidence of a Three-Nucleon Interaction

By
Christopher M. Wells
Submitted to the Department of Physics
on May 13th, 2005 in partial fulfillment of the requirement for the
degree of Bachelor of Science

Abstract

A series of experiments has been performed at the Los Alamos Neutron Science Center (LANSCE) by collaborators from the Los Alamos National Laboratory (LANL), the Massachusetts Institute of Technology, the University of Kentucky and Houghton College to examine the possible role of a three nucleon force (3NF) in the strong nuclear interaction. From 1998 to 2002 neutron-deuteron elastic scattering d(n,nd) cross sections were measured in the kinematical region predicted by theory to be most sensitive to contributions from a 3NF. The results of that study motivated measurements of the breakup reaction, d(n,np)n, which theoretical predictions suggested might be even more sensitive to 3NF effects. In each experiment, spallation neutrons were scattered from a liquid deuterium target and outgoing particles were incident on an array of neutron and charged particle detectors. Until 2003, outgoing protons were detected with CsI crystal scintillators and neutrons by either plastic or liquid scintillation detectors. In 2004, several changes were proposed for the detection array, including two permanent magnet charged particle spectrometers and large plastic scintillator bars to detect neutrons. These changes addressed problems discovered in the spring of 2003 with both the experimental setup and the theoretical calculations. Preliminary reaction cross-section results have been obtained for the d(n,nd) reaction, and the d(n,np)n cross-section measurement is planned to begin in August 2005.

Thesis Supervisor: Dr. Mark Yuly

Title: Professor of Physics

TABLE OF CONTENTS

TABLE OF FIGURES

Chapter 1

INTRODUCTION

1.1 History and Motivation

Since the 1970's physicists have been developing what is now called the standard model of particle physics. In this model, all matter is composed of three types of elementary particles: leptons, quarks and exchange particles called gauge bosons which mediate the forces. Table 1 is a summary of the standard model. There are six leptons: the electron, muon, tau and their associated neutrinos. The leptons interact via the electromagnetic and weak forces. The exchange particle for the electromagnetic force is of course the photon and the weak force is mediated by the heavy (on the order of 100 GeV/c^2) W and Z bosons. The quark family also has six members: up, down, charm, strange, top and bottom. Quarks interact via all three of the forces of the standard model, including the hadronic or strong nuclear force [1].

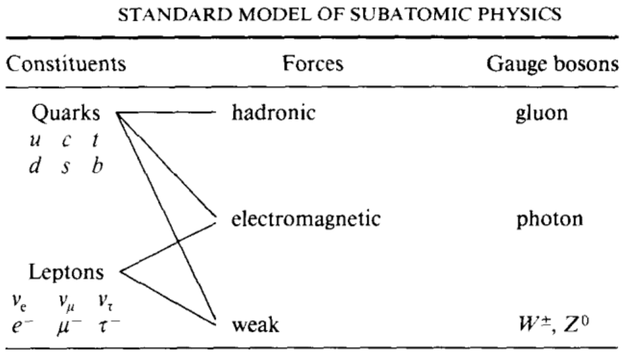

STANDARD MODEL OF SUBATOMIC PHYSICS

Constituents	Forces	Gauge bosons
Quarks u c t d s b	hadronic	gluon
	electromagnetic	photon
Leptons ν_e ν_μ ν_τ e^- μ^- τ^-	weak	$W^\pm, Z^0$

Table 1. Summary of the standard model of particle physics. In the standard model all matter is made up of quarks, leptons and force mediators (gauge bosons). Taken from Ref. [1].

The best theoretical model for the strong force, at present, is Quantum Chromodynamics (QCD). The 'chromo' in QCD refers to the degree of freedom called color for quarks and the gluons which mediate the strong interaction between them. In electromagnetism, the exchange bosons, i.e. photons, do not interact directly with each other. Gluons, however, are 'color-charged.' This means that the gluons can interact with quarks and can also interact with one another. This makes QCD fundamentally non-linear and hence difficult to solve. QCD predicts a squared coupling constant for the strong force that becomes increasingly larger as the momentum transfer of an interaction decreases, or in other words, as the distance scale probed increases. This leads to a phenomenon known as "quark confinement." As two quarks are separated, more and more energy is stored in the strong field and eventually there is enough energy to create more quarks [1]. For this reason, at comparatively low nuclear energies, it is very difficult to use QCD to make predictions of measurable quantities. Attempts have been made to empirically fit the strong force potential to scattering and binding data. See Ref. [2] for a description of several attempts.

1.2 Description of the three-nucleon interaction

Most of the effective potentials that have been proposed are based on a two nucleon model for the strong interaction, e.g. the CD Bonn potential [3]. See also Refs. [2], [4] and [5] for further discussion of a number of other 2NF models.

A two-body interaction, like gravity or the Coulomb force, acts between pairs of bodies, so that in a group of bodies the force on any of them can be explained in terms of forces between pairs. Figure 1 is an illustration of an attractive central two body interaction.

Figure 1. Drawing of a two body interaction In this example of an attractive, central two body interaction, the force draws the two interacting bodies along the line connecting their centers. However, it is not necessarily the case that a two body interaction be attractive or act centrally.

Generally, a two body interaction could depend on a variety of physical parameters, e.g. separation, spin and relative angular momentum, see Eq. 1. The parameters for two nucleon potentials are generally fitted to np and pp scattering measurements, see Ref. [2]. As an example of a very general two nucleon potential energy, consider the following for nucleons 1 and 2:

$$V_{NN} = V_C + V_{SC}\boldsymbol{\sigma}_1\bullet\boldsymbol{\sigma}_2 + V_T S_{12} + V_{LS}\mathbf{L}\bullet\tfrac{1}{2}(\boldsymbol{\sigma}_1 + \boldsymbol{\sigma}_2). \qquad (1)$$

V_C is the typical central potential term, similar to the potential energy for a system of two point charges interacting via the Coulomb force. V_{SC} is also a central term, however, it does not depend on the separation between the nucleons, it depends on their spins; $\boldsymbol{\sigma}_1$ and $\boldsymbol{\sigma}_2$ are the spin operators for nucleon 1 and 2. V_T is the tensor force and is a non-central force analogous to the interaction between two electric dipoles. S_{12} is the tensor operator, given by:

$$S_{12} = 3(\boldsymbol{\sigma}_1\bullet\mathbf{r})(\boldsymbol{\sigma}_2\bullet\mathbf{r}) - \boldsymbol{\sigma}_1\bullet\boldsymbol{\sigma}_2. \qquad (2)$$

This force depends essentially on the angle between the spins of the interacting nucleons and the vector that connects them, $\mathbf{r}$. The final term in Eq. (1) is V_{LS} which arises from the interaction of the relative orbital angular momentum Eq. (3) of the nucleons and their spin angular momentum:

$$\mathbf{L} = \tfrac{1}{2}(\mathbf{r}_1 - \mathbf{r}_2)\times(\mathbf{p}_1 - \mathbf{p}_2). \qquad (3)$$

The relative contributions of each of the V_i in an effective potential are fixed by a combination of theoretical calculations and empirical data.

When these 2NF models are used to make predictions about systems of three or more nucleons, some problems arise. For example, there is a disagreement between predicted and measured d(n,nd) cross-sections [6]. Figure 2 is a plot of proton deuteron scattering cross section measurements and the cross section as calculated with the CD Bonn two nucleon potential. Notice the difference between theoretical and experimental values, especially at the cross section minimum.

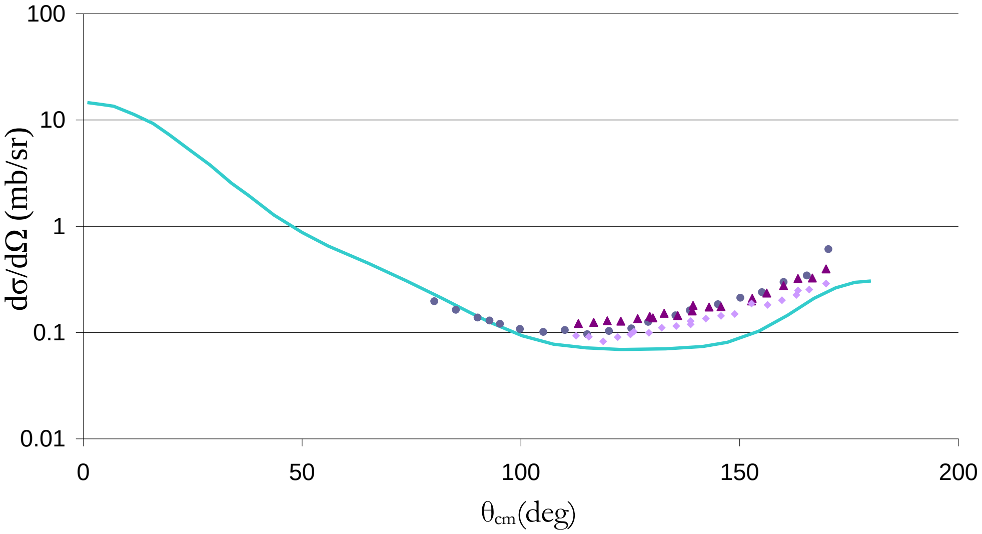

Figure 2. Measured pd scattering cross sections and d(n,nd) predictions made with the CD Bonn 2NF at an incident neutron energy of 200 MeV (light solid line) [5]. The pd data are 181 MeV (▲) from [7], 216.5 MeV (♦) from [7] and 198 MeV (●) from [8]. θ_{cm} is the deuteron scattering angle measured from the beam line in the center of mass. Observe the difference between theory and experimental cross sections, especially at the cross section minimum. Plot taken from Ref. [26].

It has been suggested [6] that discrepancies such as those mentioned above can be explained by the existence of a three nucleon force (3NF) component [9, 10]. The 3NF is a type of three body interaction. As illustrated in Figure 3, a 3NF only acts when three nucleons are present.

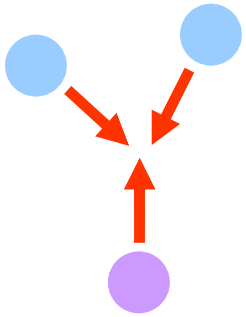

Figure 3. Drawing of a three body interaction. A three body interaction acts on particles (represented by filled circles) in groups of three and is distinct from two body interactions between particles.

The 3NF component cannot be explained in terms of multiple two-nucleon interactions. The measured binding energy of the ^{3}H nucleus has been used to parameterize the 3NF component [11], for example, the Tucson-Melbourne (TM) 3NF is based on a two pion exchange model and its parameters are fitted to ^{3}H binding data [12]. TM has been used to make predictions of the d(n,nd) and d(n,np)n reaction cross-sections. The experiments described in this paper are designed to test those predictions.

1.2.1 Cross Sections

Before the comparison of 2NF and 3NF model predictions with experimental measurements can be discussed, the concept of cross section must be developed. Figure 4 shows how the cross section arises from other measurable quantities in a reaction. The reaction cross-section is a quantity defined by:

$$d\mathcal{N} = FN\sigma(\theta)d\Omega, \qquad (1)$$

where d$\mathcal{N}$ is the number of scattered particles, F is the flux of the incident particle beam and N is the number of scattering centers in the target. The detector solid angle is Ω, measured in steradians (sr) and given by:

$$\Omega = \int \frac{dA}{r^2}, \tag{2}$$

where A is the area of the detector. If the detector was a spherical shell surrounding the target, then Ω would be 4π sr. The coefficient of proportionality $\sigma(\theta)$, is the differential cross-section as a function of the scattering angle θ, as shown in Figure 4.

Usually this is denoted:

$$\sigma(\theta) = \frac{d\sigma}{d\Omega}(\theta). \tag{3}$$

Hence, the total number of scattered particles is:

$$\mathcal{N} = FN\sigma_{tot} \text{ where } \sigma_{\text{tot}} = \int \sigma(\theta) d\Omega, \tag{4}$$

integrated over all solid angles [13].

All of the preceding applies to what is a called a singly differential cross section. If both of the scattered particles are detected, as in d(n,nd), then $d\mathcal{N}$ is expressed in terms of the detection solid angles for both outgoing particles. The corresponding cross section is termed doubly differential:

$$\sigma(\theta_1, \theta_2) = \frac{d^2\sigma}{d\Omega_1 d\Omega_2}(\theta_1, \theta_2). \tag{5}$$

The cross-section can depend on a number of kinematical quantities such as scattering angles, incident particle energy and/or scattered particle energies. It does not, however, depend on the specifics of a given experimental setup, but only on the "physics" of the scattering reaction, and consequently can easily be compared to other experimental results and used to test theoretical predictions.

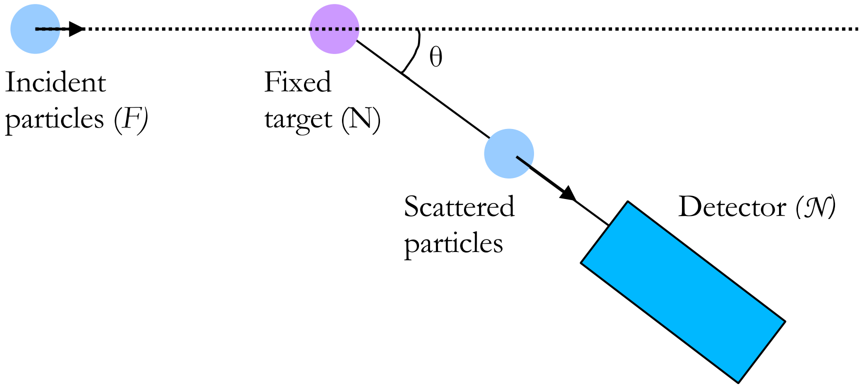

Figure 4. Diagram of a particle scattering from a fixed target. The number of scattered particles (𝒩) detected at an angle θ is proportional to the incident particle flux (*F*) and the number of scattering centers in the target (N). The proportionality constant is the total cross section σ(θ).

1.2.2 The d(n,nd) Reaction

Obviously, to test the predictions of 3NF potentials it is necessary to study reactions involving at least three nucleons. One simple reaction belonging to this category is d(n,nd), because it involves two neutrons and one proton. This reaction has the advantage over d(p,pd), for example, because it does not include large contribution due to Coulomb scattering.

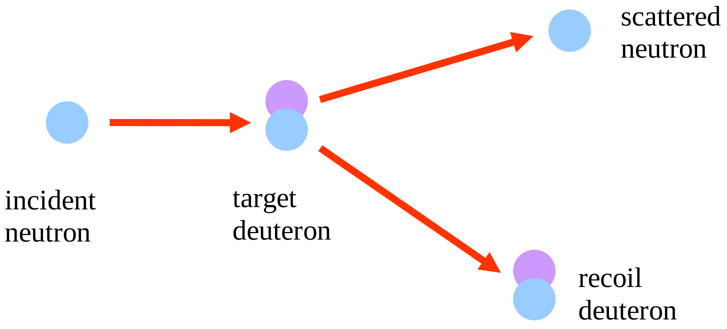

Figure 5. Schematic representation of the neutron deuteron elastic scattering reaction d(n,nd). A neutron is incident on a target deuteron, the particles scatter and both are detected. The neutron's initial kinetic energy is conserved.

As can be seen in Figure 5, in the d(n,nd) reaction, a neutron is incident on a target deuteron resulting in a scattered neutron and a recoil deuteron, both of which are detected. The deuteron is a barely bound state, so there are no excited states. This means that if the deuteron is not broken up by the incident neutron, the scattered neutron and deuteron will share the neutron's kinetic energy and scatter elastically. The theoretical predictions for the d(n,nd) cross-section made with the strictly two-nucleon CD-Bonn strong potential differ from those including the TM 3NF component. This can be seen in Figure 6, which compares the cross-section predictions for scattering 200 MeV neutrons from a deuterium target with proton-deuteron scattering cross section measurements at incident proton energy around 200 MeV.

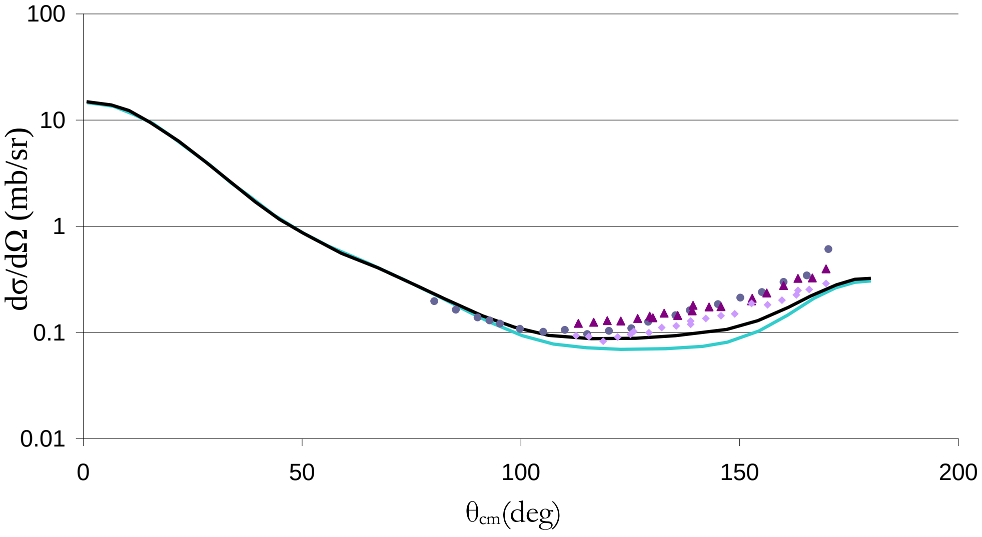

Figure 6. Plot of pd scattering cross sections and d(n,nd) cross section predictions at 200 MeV incident neutron energy made with the CD Bonn 2NF (light solid line) [5] and 2NF plus TM 3NF [9] (dark solid line) potentials. The pd data are 181 MeV (▲) from [7], 216.5 MeV (♦) from [7] and 198 MeV (●) from [8]. θ_{cm} is the deuteron scattering angle measured from the beam line in the center of mass. Observe the difference between 2NF and 3NF predictions, especially at the cross section minimum. Plot taken from Ref. [26].

1.2.3 The d(n,np)n Reaction

Another comparatively simple three-nucleon reaction is neutron induced deuteron breakup, d(n,np)n. In this case an incident neutron interacts with the target deuteron splitting it into its constituent neutron and proton, as in Figure 7.

Theoretical predictions [15] suggest that the d(n,np)n cross-section is very sensitive to the presence of a 3NF component. Figure 8 is a contour plot of the enhancement to the d(n,np)n cross-section upon inclusion of the TM 3NF component. Because the d(n,np)n reaction is less kinematically constrained than d(n,nd). Since the energy is shared by three outgoing particles, the cross section is expressed as a five-fold differential. Notice that the greatest enhancements, i.e. the darkest portions of the contours, are at forward scattering angles - $\theta_{1,2} < 50°$. There is an especially large region of enhancement at 65 MeV incident neutron energy (E_n) and $\varphi_{12} < 75°$. There are also noticeable enhancements at large scattering angles, i.e. $\theta_{1,2} > 100°$, for $E_n = 135$, 200 MeV. For $E_n = 135$ MeV, $\varphi_{12} \approx 20°$ and $\theta_1 \approx 20°$ the percent enhancement is almost 90%.

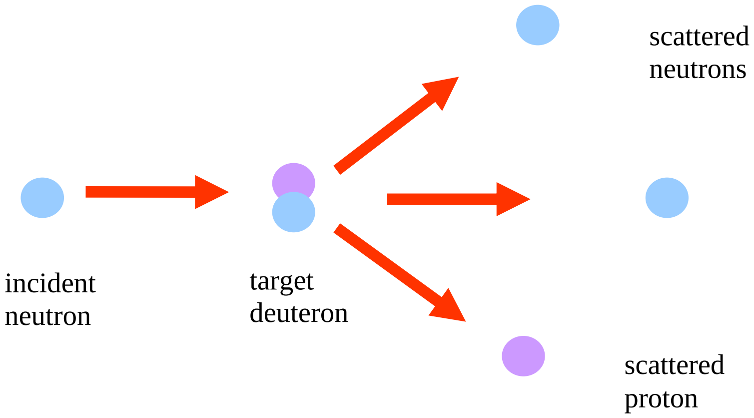

Figure 7. Schematic representation of the d(n,np)n reaction. In this reaction the incident neutron breaks the target deuteron into a neutron and a proton. The signature for this reaction is the detection of a neutron and a proton in coincidence.

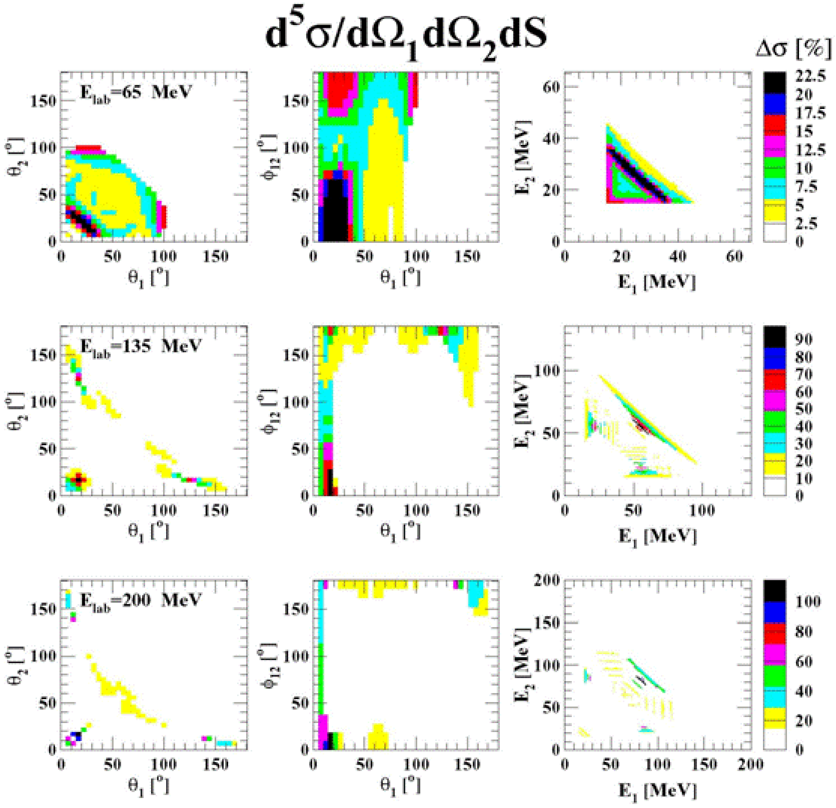

Figure 8. Two-dimensional projections of calculated cross-section enhancements for nd-breakup at 65, 135 and 200 MeV. $\Delta\sigma$ is the absolute difference between the 2NF and 2NF + 3NF predictions. E_1, θ_1 and E_2, θ_2 are the neutron and proton energies and scattering angles in the center of mass frame in the reaction plane. φ_{12} is the angle between the nucleon trajectories out of the beam plane. For example, $\varphi_{12}= 180°$ indicates that the scattered nucleons end up on opposite sides of the beam line. These predictions were calculated with the CD Bonn 2NF [15] + Tucson-Melbourne (TM) 3NF [12]. The color scale indicates the percent enhancement to the cross-section, with darker colors indicating greater enhancement. Finally, the cross-section section enhancement is expressed as a function of 'S', a quantity with units of energy that depends on the specific kinematics of the breakup configuration; see Ref. [14] for a discussion of the 'S' formalism. Plot taken from Ref. [15].

Chapter 2

DESIGN OF EXPERIMENTS

2.1 Overview

From 1998-2004 a number of experiments were carried out at the Weapons Neutron Research (WNR) Facility of the Los Alamos Neutron Science Center (LANSCE) to measure first the d(n,nd) cross-section and then the d(n,np)n cross-section.

2.2 LANSCE

LANSCE is a part of the Los Alamos National Laboratory (LANL) and is situated on top of a mesa in Los Alamos, NM (see Figure 9). It replaced the former Los Alamos Meson Physics Facility (LAMPF) which produced pion beams. LANSCE relies on the Clinton B. Anderson linear accelerator (LINAC) which provides a 1 mA, 800 MeV proton beam for a variety experiments in nuclear physics. The WNR facility was constructed adjacent to the beam line (see Figure 10) to utilize the high intensity beam at LANSCE for weapons design research and fundamental nuclear physics research.

2.3 The LINAC

The LINAC at LANSCE produces one of the highest power proton beams in the world at 1 MW with an average proton current of up to 1 mA at 800 MeV. The beam produced at LANSCE is particularly well-suited to these experiments because it is a 'white source,' hence a spectrum of incident neutron energies can be examined at once. All of the experiments were located at WNR which has two spallation neutron production targets, Target 2 and Target 4. Target 4 supplied the incident neutron beam for these experiments and is, "the most intense high-energy neutron source in the world." [16]

Figure 9. Aerial photograph of LANSCE taken from Ref. [16]. The series of buildings that house the side coupled linac cavities is visible on the left. The proton storage ring (PSR), where proton beam pulses are compressed, can be seen next to the WNR, where the d(n,nd) and d(n,np)n measurements took place.

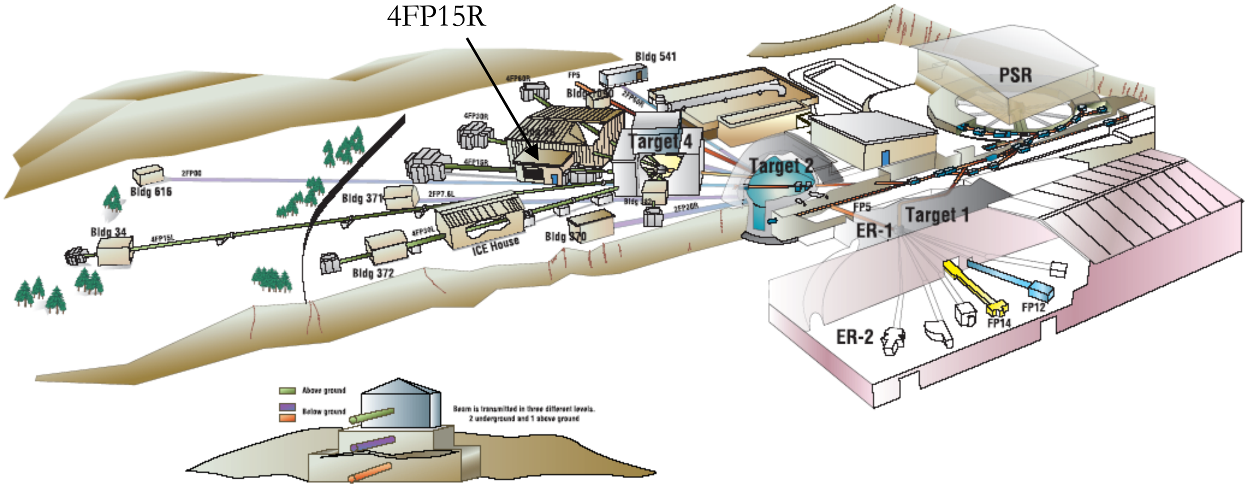

Figure 10. Drawing of the WNR facility. The proton beam is bent under the road at the top right and enters the PSR where it is compressed. It then travels to spallation target 4 located near the center of the drawing. Just downstream from target 4 is experimental area 4FP15R. Taken from Ref. [16].

The protons begin in one of three ion injectors at LANSCE (Figure 12). Each injector consists of a 750 kV Cockcroft-Walton accelerator and an ion source capable of producing both H^+ and H^- ions. The ions leave the injectors at 750 keV and enter the drift-tube LINAC. The drift-tube LINAC is approximately 62 meters long and its electric field alternates at 201.25 MHz. The alternating electric field allows the acceleration of positive and negative ions simultaneously. Ions are alternately 'pushed' and 'pulled' by the rapidly oscillating potential on the drift tubes. The successive tubes become increasingly longer to compensate for the acceleration of the ions until relativity makes this sort of compensation ineffectual. The ions leave the drift tube linac at 100 MeV and enter a side-coupled cavity LINAC (which functions in much the same way as the drift-tube LINAC) where they are accelerated through 4800 individual drift cells up to their final energy of about 800 MeV.

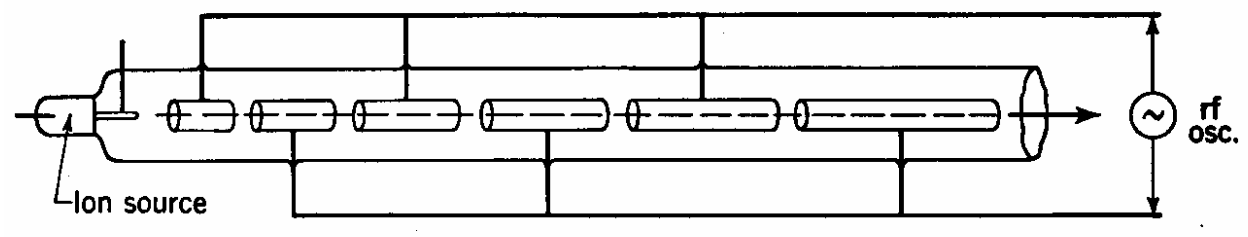

Figure 11 Schematic of a typical drift tube LINAC. Ions are 'pushed' and 'pulled' by the alternating potential on the increasingly long drift tubes. Taken from [31].

Figure 12. Photograph of one of the Cockroft-Walton injectors at LANSCE which inject H^+ and H^- ions into the LINAC at 750 keV. Taken from Ref. [16].

2.4 The Neutron Beam

The full energy proton beam then enters a switchyard where it is directed to several different targets. The maximum average current for the proton beam is 0.8 mA and the beam is divided into 900 μs macropulses. The macropulses are further divided into 0.25 ns micropulses separated by 5 ns [17].

The H^+ proton beam enters a proton storage ring (PSR), where the long proton pulses are compressed into the 270 ns pulses that are delivered to the tungsten spallation target. The proton beam strikes the tungsten target and neutrons are scattered with a spectrum of energies in every direction. Some of these neutrons are collimated with heavy lead and concrete shielding into various beam lines which lead to experimental areas (Figure 10). Neutron energy at the target in the experimental area is calculated using the time of flight from the spallation target to the liquid deuterium target, a distance of about 18 meters. Thus, the duration of a proton beam pulse determines the overall incident neutron energy resolution. All of the experiments were located along WNR flight path 4FPR15, 15° to the right of the beam line from spallation target 4. Plotted in Figure 13 is the neutron flux at 15°, 30°, 60° and 90° on either side of the beam line.

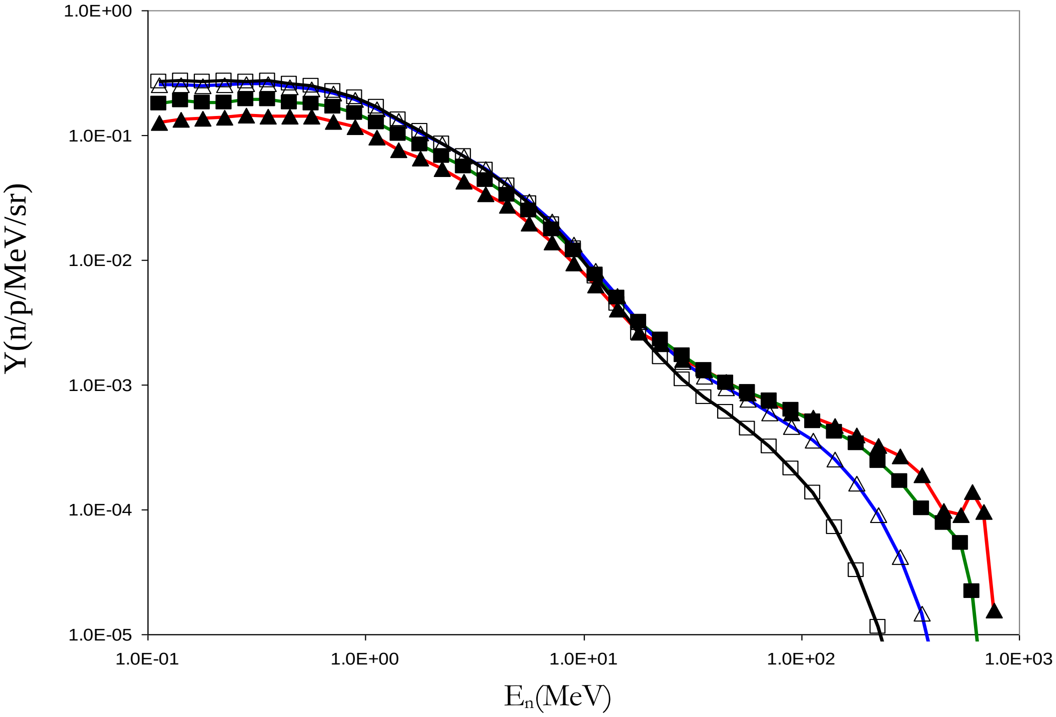

Figure 13. Plot of neutron flux at the WNR experimental areas per incident proton per MeV per steradian at four scattering angles: (▲) 15°, (■) 30°, (△) 60° and (□) 90°. The neutrons are the result of the spallation reaction between the 800 MeV protons and tungsten target 4.

2.5 Target

The d(n,nd) and d(n,np)n measurements used the same target set up to contain the target deuterons or protons. The liquid deuterium target itself was a 12.7 cm diameter by 1.3 cm thick cylindrical flask, see Figure 16. On either end of the target is a very thin (2 mm) mylar window. The target could be filled with either liquid deuterium or liquid Hydrogen. The latter was useful for collecting np scattering data which could be used for normalization of the d(n,nd) and d(n,np)n measurements.

This entire assembly was placed inside of a vacuum chamber which provided thermal insulation for the liquid target. The vacuum chamber itself was an approximately 32 cm diameter vertical cylinder of 0.48 cm thick stainless steel. The chamber had a 5 mm kapton window which provided an opening to approximately 180° of scattering angle. The target window and vacuum equipment can be seen in Figure 14.

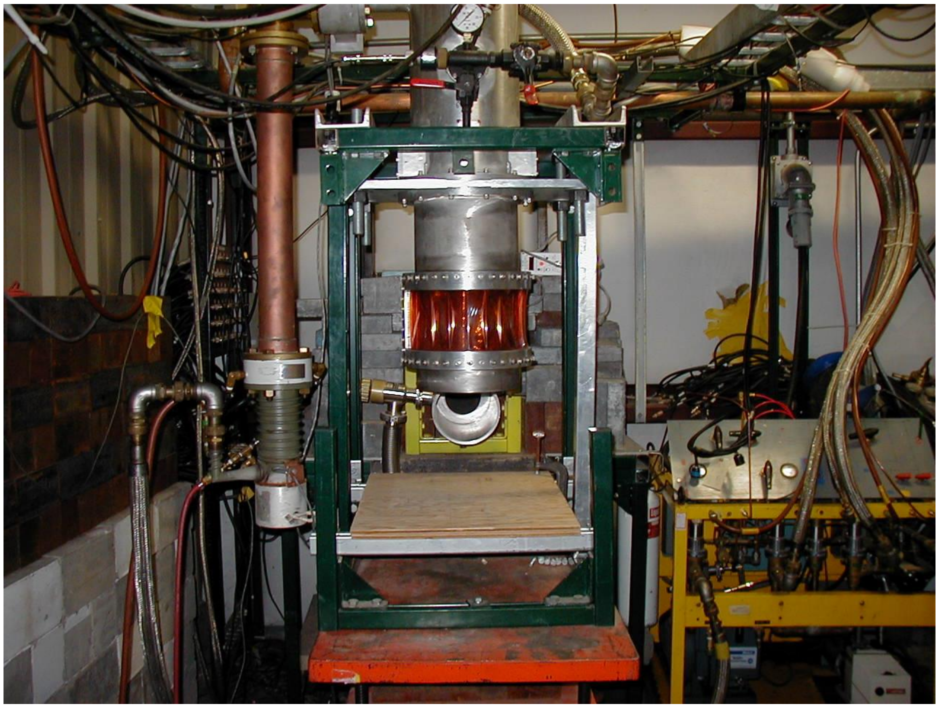

Figure 14. Photograph of the liquid deuterium target chamber. The target has been raised above the beam pipe in the center. The vacuum system for the target chamber is on the right.

Figure 15 is a diagram of the cryogenic system used with the liquid deuterium target. The main component is a CTI Model 1020 cooler with a cooling capacity of 10 Watts at 20 K. The Nitrogen trap and oxygen filter are in place to purify the gas (hydrogen or deuterium) before it is liquefied in the condensing chamber. A simple resistor based heater was used to control the pressure [30].

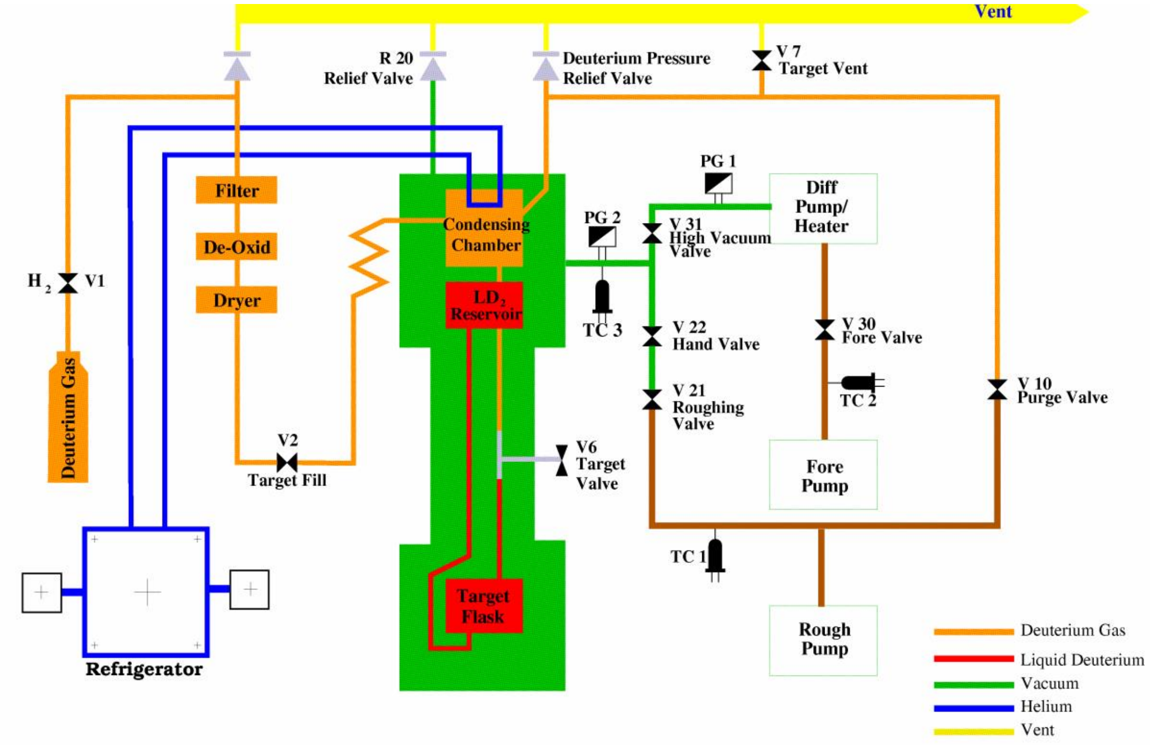

Figure 15 Diagram of the liquid deuterium target and refrigeration system. The orange sections indicate the presence of deuterium Gas. The red sections indicate the presence of liquid deuterium. The green indicates vacuum, blue indicates helium and the yellow sections indicate a vent. Plot taken from Ref. [30].

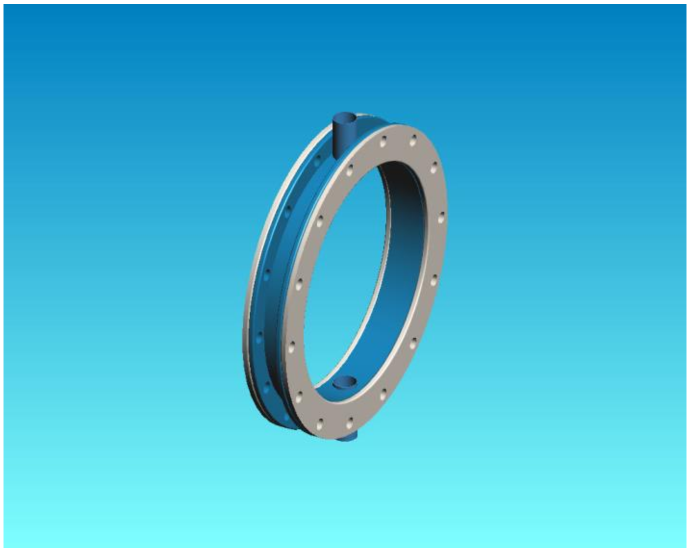

Figure 16. Drawing of the cylindrical target flask, taken from Ref. [30]. This design was used in the 2001 experiment and those that followed.

2.6 Fission Chamber

Calculating the cross sections from d(n,nd) and d(n,np)n measurements requires knowledge of the flux of incident neutrons. In all of the experiments at LANSCE, a fission chamber, located between the beam pipe and the LD_2 target, was used to measure the incident neutron flux [18]. The housing for the fission chamber was an aluminum cylinder 29.2 cm in diameter and 9.5 cm in length. The actual ionization chamber was 14 cm smaller in diameter in order to reduce background counts due to neutrons on the outside edges of the beam. The windows of the chamber were 0.025 cm thick stainless steel sealed to the chamber with neoprene "O" rings. The foils, visible in Figure 17, had deposits of ^{238}U and ^{235}U that fissioned for a certain fraction of incident neutrons. The ^{235}U fissions when struck by neutrons with energy slightly below 1 MeV and up to 500 MeV. A certain fraction of the resulting fission fragments made it to the foils which were kept at a high negative bias (around -300V) and hence produced a signal when stuck by a fission fragment. The number of output pulses was therefore proportional to the incident neutron flux [19].

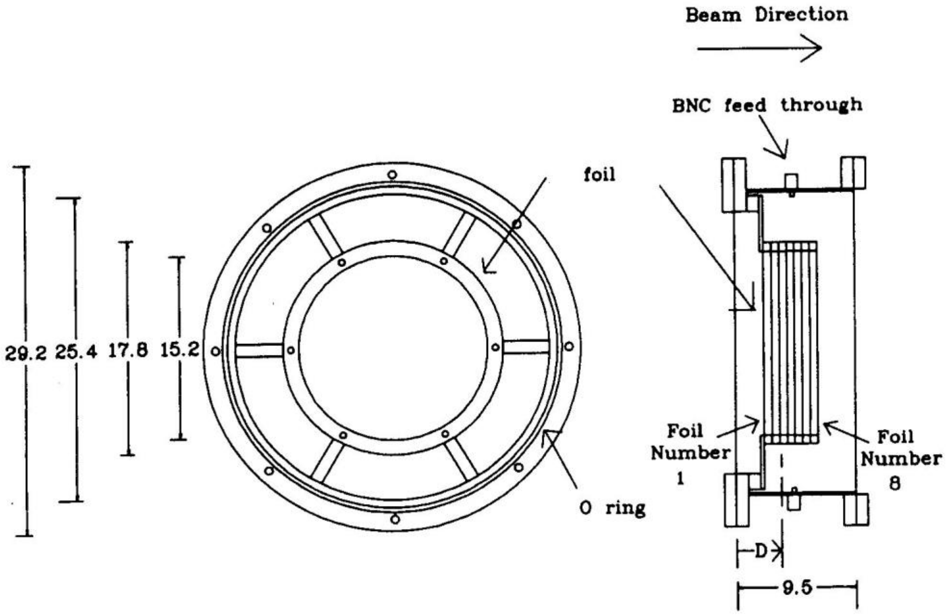

Figure 17. Schematic diagram of the fission ionization chamber used to measure neutron flux. Taken from Ref. [18].

2.7 Electronics

The signals from the detectors in the experimental area were processed by a data acquisition circuit. A detailed circuit diagram for each of the experiments can be found in Appendix C. However, all of the experiments described in this paper used very similar logic for triggering the computer to read out data which is shown in a greatly simplified logic diagram in Figure 18.

In each of the reactions studied, the signature for an event was the detection of two particles in coincidence – in d(n,nd) a neutron and deuteron in coincidence and in d(n,np)n a neutron and proton. In Figure 18, the signals from charged particle detectors (whether used to detect protons or deuterons) are represented by the yellow block and the neutron detector signals are represented by the red block. The T_0 module is the signal that came from the accelerator to indicate when a beam pulse occurred. The computer was triggered to read in data on two main types of events: charged particle-neutron coincidences and a certain fraction of single events. A single event occurs when, for example, a charged particle detector is set off without a simultaneous event in a neutron detector. The coincidence unit ('and' gate) in the center of the schematic, labeled "P•N", produced a signal whenever a neutron, charged particle and beam pulse arrived in coincidence. The rate dividers (RD) produced a signal on a user defined fraction of all the input pulses they receive. This information was used to determine the number of neutron and charged particle single detection events.

The "Busy OR" circuit made it impossible to trigger the computer to read in data within a certain amount of time after the last trigger. The trigger was also "vetoed" when the computer memory was full or when the rug gate (RG) was set by the user to discontinue data acquisition.

The detector pulse heights and delay times were digitized by *computer automated measurement and control* (CAMAC) modules and *analog to digital converter* (ADC) FERA modules. FERA was used because it is much faster than CAMAC. From the CAMAC and FERA modules the data were read into a dual processor Xeon computer running Red Hat Linux 7.0 [17]. The data acquisition software consisted of a "Midas" data acquisition code running on one processor and an analyzer written using ROOT classes for histogramming on the other. The raw data were stored on DVD until off-line analysis could be undertaken.

2.8 Nitrogen Laser

It is possible that after the detectors have been set up and calibrated that their gains could wander. A nitrogen laser was used to monitor the gain on each detector during the experiments at LANSCE. A fiber optic cable was connected to each detector and while the experiments were running the laser supplied a rapid pulse at a characteristic energy. This pulse showed up on pulse height histograms for each detector. A drift in the corresponding peak indicated how much the detector had shifted. This shift could then be accounted for in analysis.

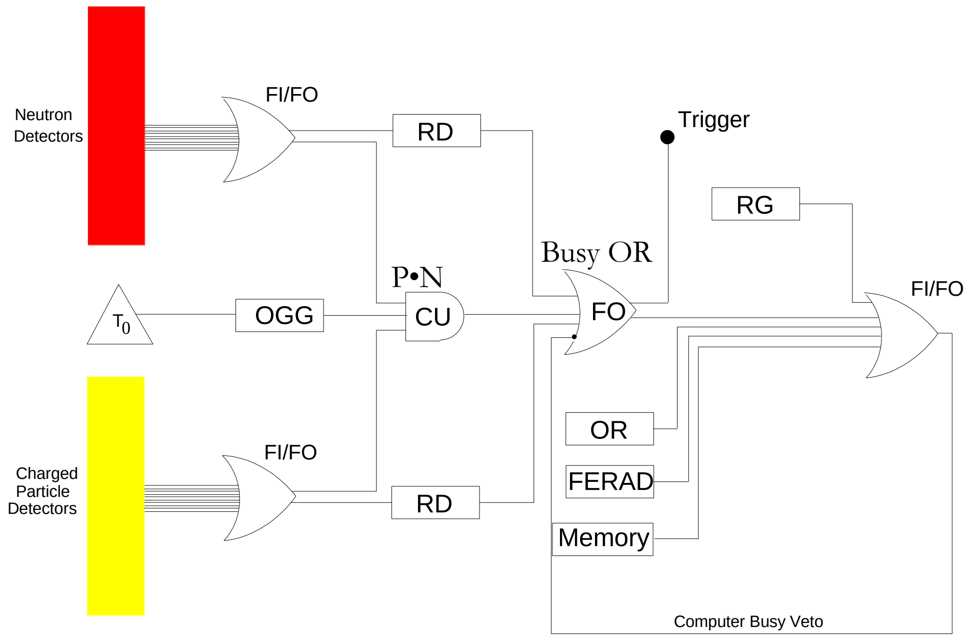

Figure 18. Simplified schematic of the circuit used to trigger the computer system to read out the CAMAC modules. The computer was triggered to record pulse height and time of flight information which are used to determine charged particle and neutron energies respectively. Triggers occured on a certain fraction of charged particle and neutron single events, determined by the rate divider. A trigger occured every time there was a coincidence between a beam pulse (indicated by T_0), a neutron detector and a charged particle detector. If the computer was busy then the trigger was vetoed.

Chapter 3

MEASUREMENTS OF THE D(N,ND) REACTION

Between 1998 and 2002 a series of experiments were performed at LANSCE to measure d(n,nd) cross sections in order to test the predictions of the 3NF model [6,11,14]. Those experiments are described below.

3.1 Initial Efforts (1998 – 2000)

The first proposal for the use of the LANSCE facilities to make a measurement of the elastic scattering cross-section was submitted in March of 1998 [20]. This proposal called for one week of beam time on 4FP15R, used previously for a very similar experiment measuring neutron-proton bremsstrahlung [21]. As calculated in the proposal, this amount of time would allow the experiment to be set up and 10% statistics to be collected at one angle. The intent of this initial experiment was to assess potential difficulties and systematic uncertainties associated with this sort of measurement. Data were not actually taken, however, until August of 2000 under a new proposal made to the LANSCE Program Advisory Committee [22].

3.1.1 Detectors

The final state of the d(n,nd) reaction is a scattered neutron and a recoil deuteron. Hence, this experiment was designed to detect a neutron and deuteron in coincidence. By requiring that a neutron and a deuteron be detected rather than simply a coincidence between a neutron detector and a charged particle scintillator, background counts from the d(n,np)n process were eliminated.

As can be seen in Figure 20, deuterons were detected with CsI crystal scintillators. The front face of the CsI scintillators was a 9.4 cm square and the back face was a 10.2 cm square. The scintillators were 30.5 cm long. Because they detected both deuterons and protons, the charged particle scintillators had a thin (about 0.4 cm) plastic ΔE scintillator taped onto their front (target side) face. Any charged particle that entered the front of the CsI scintillator would also have to pass through a ΔE scintillator.

The ΔE's provided information which could be used to distinguish between deuteron and proton events. Particles lost energy in the ΔE detector according to the Bethe-Bloch formula (Equation 1) which relates energy loss $\frac{dE}{dx}$ to atomic number, mass and energy.

$$-\frac{dE}{dx} = \frac{4\pi n z^2 e^4}{m_e v^2}\left\{\ln \frac{2m_e v^2}{I\left[1-\beta^2\right]} - \beta^2\right\} \tag{1}$$

A charged particle will lose energy dE in a distance dx as it travels through a material and interacts with its electrons. The atomic number of the charged particle is z, the speed of the particle is v, β is the rapidity of the particle (v/c), n is the number density of electrons in the material and I is the mean excitation energy of the atoms in the material. Outgoing protons and deuterons of the same energy had different β values, and therefore lost different amounts of energy, according to Equation 1. As can be seen in Figure 19, they formed different bands on a histogram of energy versus dE/dx. Thus, these CsI-ΔE telescopes provided information that made it possible to distinguish between proton and deuteron detection. The CsI crystal scintillators were chosen because of their high density, approximately 4.51x10^3 kg/m^3 [19]. Charged particles lose energy faster in higher density materials, so it is less likely that the particle will escape through the back of the detector without depositing all of its kinetic energy. These detectors are therefore useful as calorimeters.

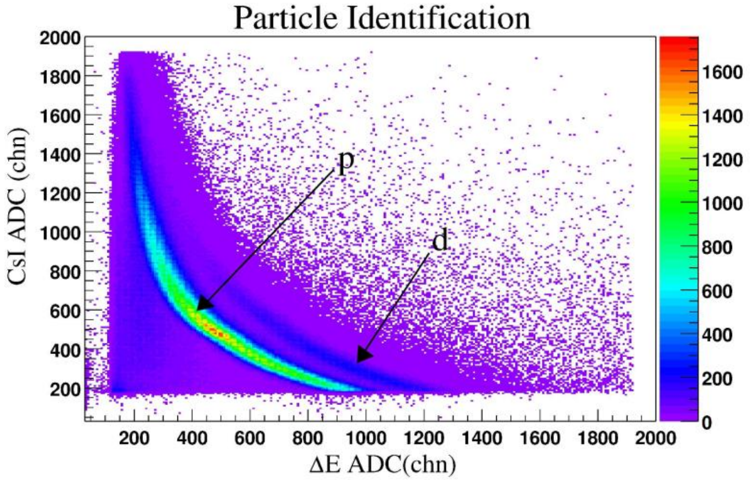

Figure 19. Histogram of E versus dE/dx in proportional units. This is a histogram of signals from the CsI scintillators plotted against the ΔE signals as read out from an analog to digital converter (ADC).

Organic liquid scintillator detectors were used to detect the neutrons; these scintillation materials are known to be efficient for detection of neutrons with energies in the MeV range [19]. Organic liquids are also known for the fast signal decay time they produce, around 3 ns [23]. This is very important for detecting neutrons, because the neutron energy resolution depends on the event timing resolution. Also, organic liquid scintillators can be used effectively to perform pulse shape analysis/discrimination. The mechanism for scintillation in a liquid scintillator is different for the detection of a photon and a neutron. Hence, a photon and a neutron will produce pulses with different decay times [23]. Electronically, a constant fraction discriminator can be used in order to separate out the pulses of various decay lengths. In order to further identify proton events in the neutron detectors, thin (about 0.8 cm) plastic 'veto' scintillators were taped to their front faces (target side). Both the veto detectors and the liquid scintillators will scintillate when a charged particle passes through them. A coincidence between a neutron scintillator and its associated veto indicated that a charged particle has been detected and the information from this event could be ignored. The veto scintillators were also set off by a certain fraction of legitimate neutron events as well. However, they were very thin, so this happened in only a small fraction of events.

The n-p scattering reaction has been studied in greater detail than n-d scattering, so after the n-d data were collected the target was filled with liquid hydrogen and the n-p scattering measurements were made for normalization of the n-d cross sections. Data were also taken with the target cell totally empty. This provided a measurement of the background count rate due to scattering off of the target housing and other equipment in the room [24]. Measurements were made with this setup during most of August 2000.

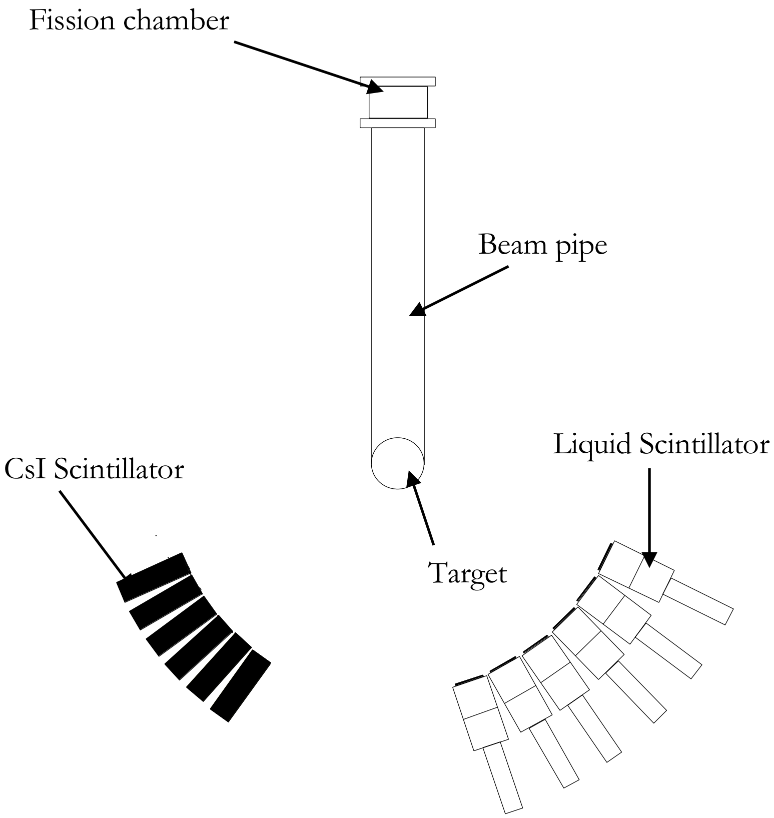

Figure 20. Simplified drawing of the experimental setup for d(n,nd) in 2000. Incoming neutron flux was measured by the fission chamber. Outgoing neutrons were detected with organic liquid scintillators. Outgoing protons were detected by CsI crystal scintillators.

3.1.2 Problems

The initial experiment report suggested that the statistical uncertainty would be less than five percent, and that this level of uncertainty would be sufficient for comparison with the 2NF and 3NF potential predictions [24]. It was believed that the accuracy would be limited by the uncertainty in the incident neutron flux, but it was discovered that the limiting factors were actually the detector efficiencies and the geometric acceptance of the detector array [25]. In setting up the detectors, calculations were made, using the charged particle detector as reference, of the conjugate angles for n-d and n-p scattering. These calculations were performed using incident neutron energy of 200 MeV. The neutron beam at LANSCE, as discussed in Section 2.3, provided a white incident neutron source with incident neutron energies ranging from about 100 MeV to almost 1 GeV (see Figure 13). The energy dependence of the conjugate scattering angles was not very strong, but because discrete detectors were used the geometrical acceptance, i.e. detection solid angle, did have noticeable energy dependence. This complicated the calculation of the experimental cross-sections because the acceptance as a function of energy needed to be known accurately. Another assumption made in calculating the scattering angles was that the n-d interactions occurred at the center of the target. However, the target was a 7.6 cm diameter cylinder. A Monte Carlo simulation based on the geometry of the 2000 experiment showed that a significant number of scattering events that occurred at the upstream and downstream edges of the target missed the detectors altogether.

3.2 Improved Design (2001 – 2002)

In 2001 and 2002 two major changes were made to the experiment: the size of the target and the type of neutron detectors, see Figure 21. The original target was a 7.6 cm diameter cylinder, oriented vertically. This was replaced with a thinner (1.3 cm thick) cylindrical target oriented with its axis parallel to the beam line. This change was made in order to reduce the number of events that were not detected due to scattering at the upstream and downstream edges of the target. The thinner target reduced deuteron energy loss in the target subsequent to the initial nd reaction. Decreasing the deuteron energy loss in the target decreased the lower limit on detectable incident neutron energies and thereby increased the energy range over which the cross-section measurement was made.

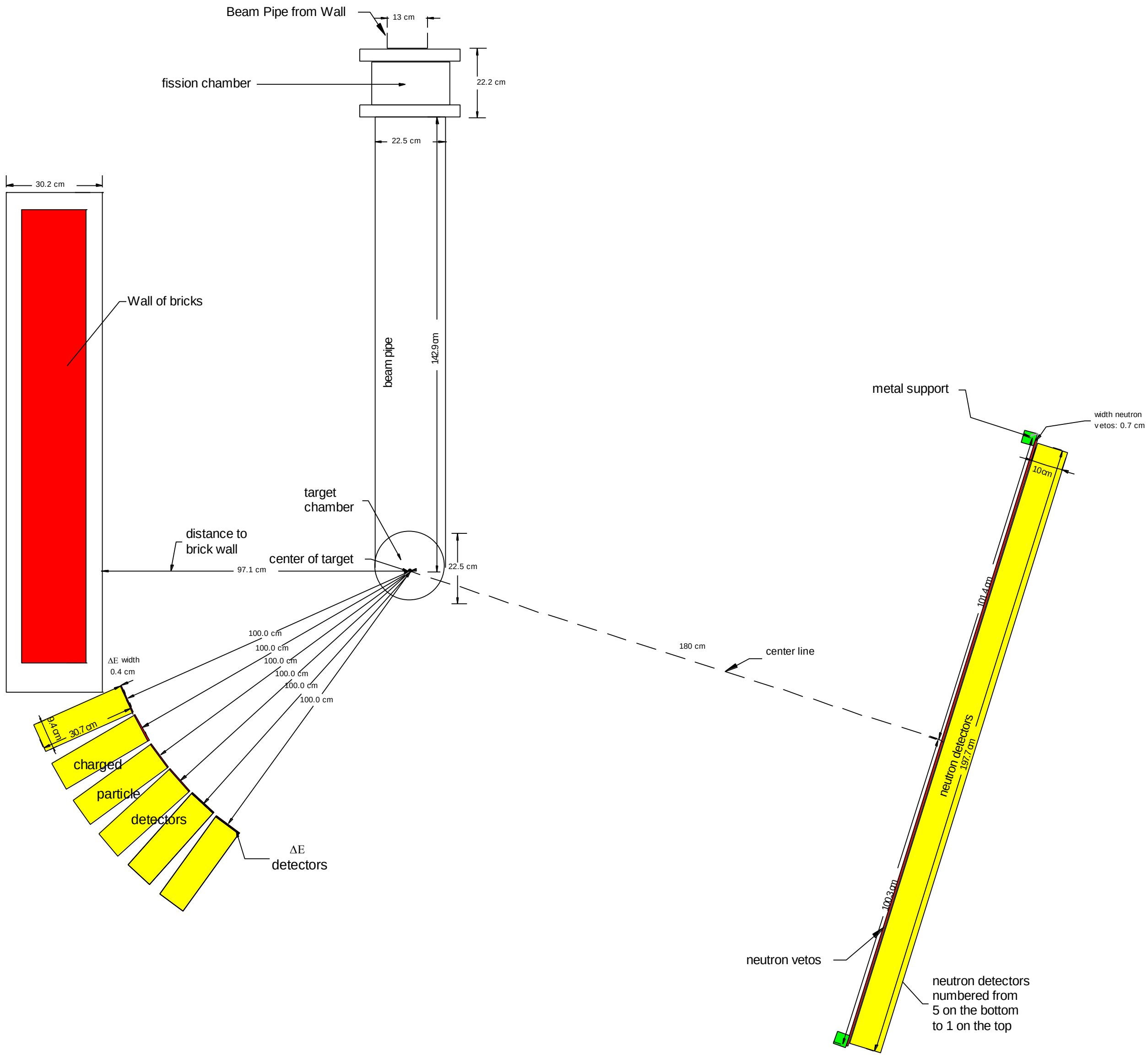

Figure 21. Schematic of the setup for the d(n,nd) experiment in 2001 and 2002. This overhead view shows the orientation of the neutron 'wall' as well as the positions of the fission chamber, target and charged particle telescopes.

3.2.1 Detectors

The other major problem was the dependence of the neutron scattering angle on incident neutron energy. The essence of the problem was that the geometrical acceptance of the discrete detectors had a strong dependence on the incident neutron energy and at energies far above or below 200 MeV the outgoing neutrons were missing the detectors [25]. The solution was replacing the discrete detectors with a "neutron wall," consisting of a stack of five plastic scintillator bars approximately 7 cm by 10.2 cm by 198 cm, each having a phototube on both ends. Generally, a flash of light in one of the neutron bars reached the ends at different times. The time difference was used to calculate the distance from the ends of the bar to the position of the event. The neutron wall was placed in such a way as to cover the entire range of neutron scattering angles conjugate to the CsI detectors for elastic scattering (see Figures Figure 22Figure 23. By covering a much larger solid angle, the problem of geometrical acceptance being dependent on neutron energy was significantly reduced. An added feature of this detection array was an increase in neutron detection solid angle and a recovery of some of the count rate lost by switching to a much thinner target [25]. CsI charged particle scintillators and ΔE scintillators were again employed in this setup. Four large (approximately 12.8 cm by 99 cm) "paddle" veto scintillators were attached to the front of the neutron "wall."

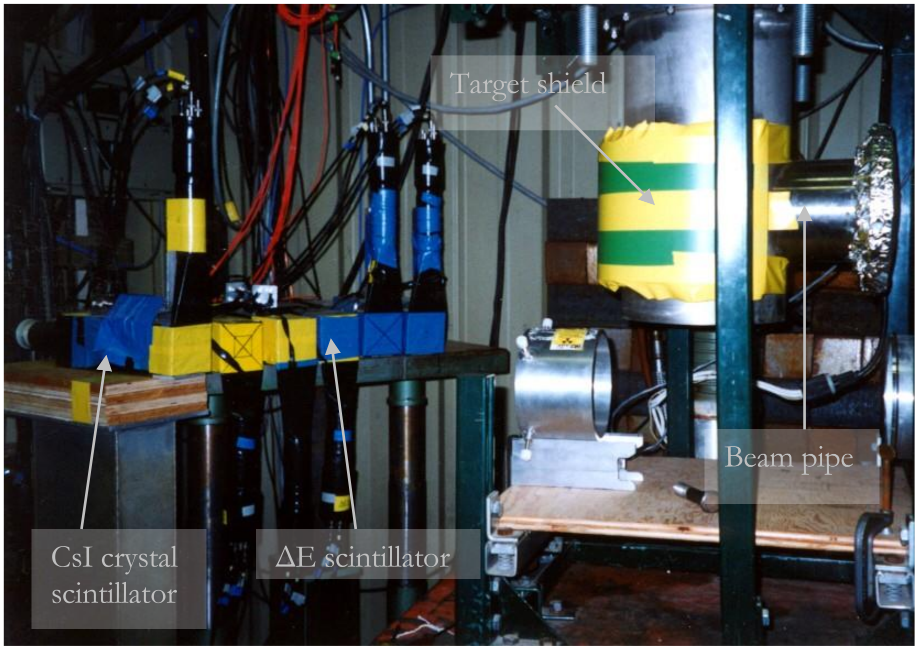

Figure 22. Photograph of the deuteron detector telescopes for d(n,nd) in 2002. The neutron beam entered the experimental area through the beam pipe at the right. Scattered deuterons were detected by the array of CsI crystal and ΔE scintillator charged particle telescopes on beam right. The target chamber was evacuated and so it was shielded in case of implosion.

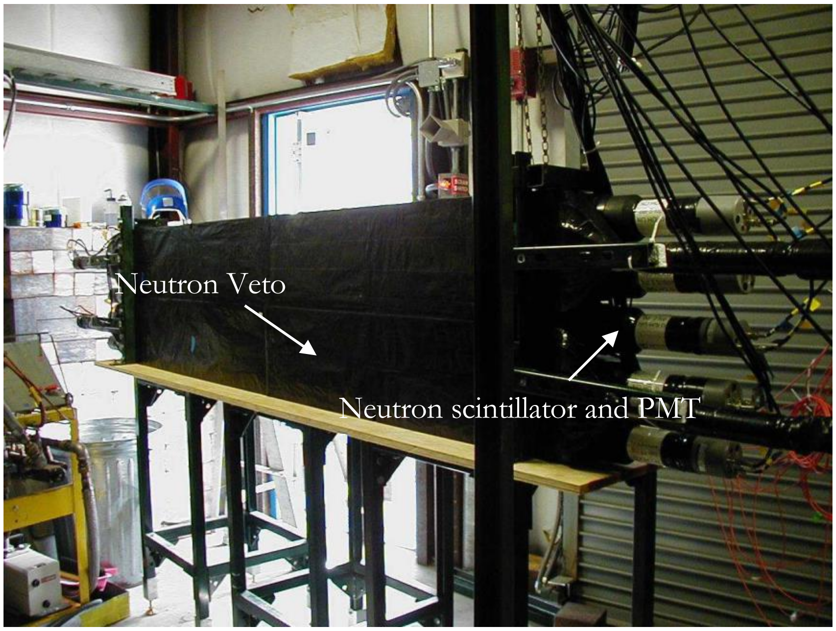

Figure 23. Photograph of the neutron 'wall' for d(n,nd) in 2002. The stack of five long plastic neutron scintillators is visible in this photograph and, though difficult to make out, the neutron veto scintillators are also visible in front of the neutron “wall”.

3.2.2 Results

The experimental scheme of Figure 21 was used successfully to make d(n,nd) cross section measurements. Figure 24 and Figure 25 are examples of cross section results at incident neutron energies of 140 and 200 MeV; further analysis at other incident energies is forthcoming [30]. As in Figure 6, there is a very clear difference between the prediction made by the purely two nucleon CD-Bonn potential [3] and the prediction made by CD Bonn with TM 3NF component [12]. The cross sections collected at LANSCE are consistent with the 3NF predictions at both 140 and 200 MeV.

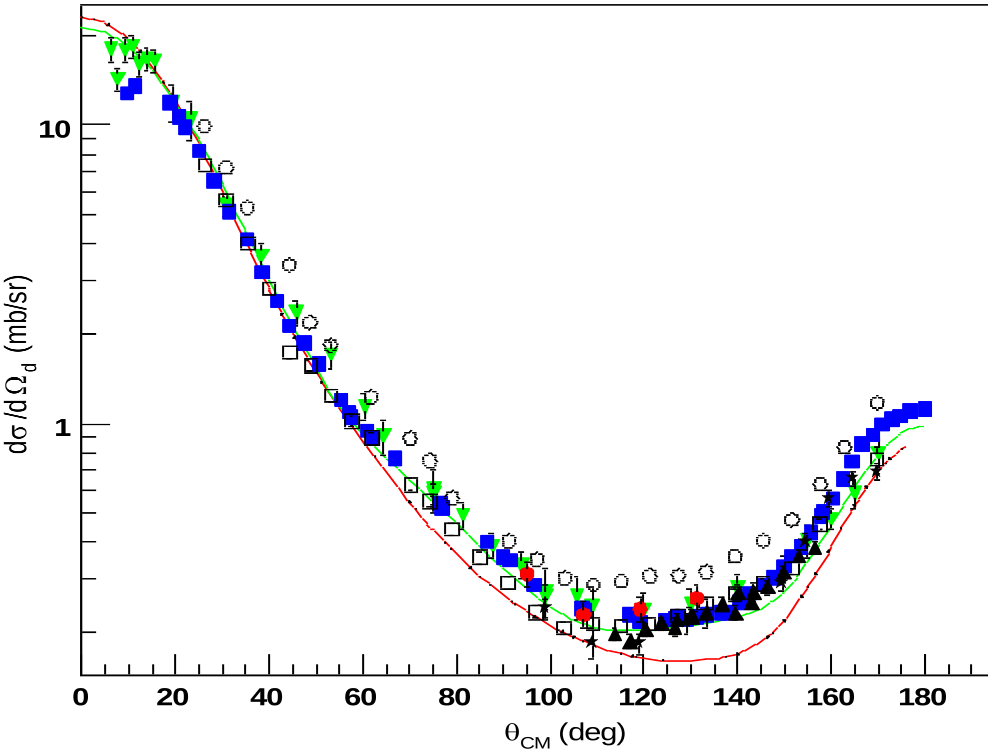

Figure 24. Plot of d(n,nd) cross-section measurements taken at LANSCE at an incident neutron energy of 140 MeV. The ● are the measurements made at LANSCE. The vertical axis is the differential cross-section for nd elastic scattering and the horizontal axis is the deuteron scattering angle in the center of mass frame. Theory curves and pre-existing data are taken from Ref. [26]. Theory predications were made with the CD Bonn 2NF (dark solid line) [5] and 2NF plus TM 3NF [9] (light solid line) potentials. The pd data are (▼) 146 MeV [27], (■) 270 MeV [28], (□) 150 MeV [29], (○) 135 MeV [29], and (▲) 291 MeV [7]. Plot taken from Ref. [30].

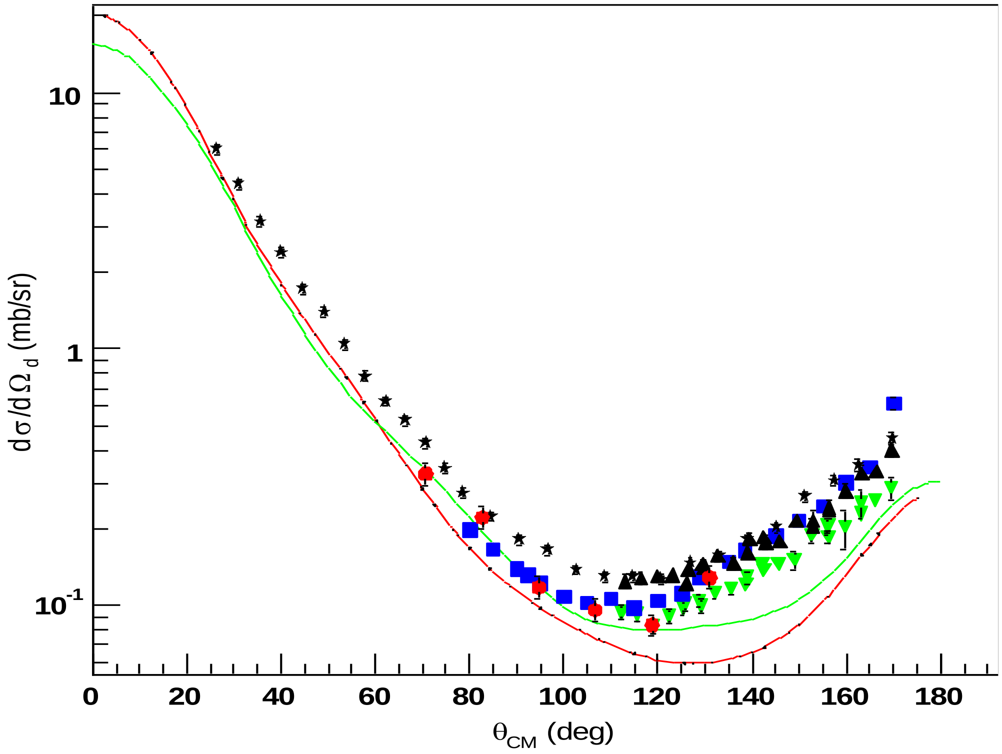

Figure 25. Plot of d(n,nd) cross-section measurements taken at LANSCE at an incident neutron energy of 200 MeV. The ● are the measurements made at LANSCE. The vertical axis is the differential cross-section for nd elastic scattering and the horizontal axis is the deuteron scattering angle in the center of mass frame. Theory curves and pre-existing data are taken from Ref. [31]. Theory predications were made with the CD Bonn 2NF (dark solid line) [5] and 2NF plus TM 3NF [9] (light solid line) potentials. The pd data are (▼) 433 MeV [7], (■) 198 MeV [8], (*) 190 MeV [29] and (▲) 362 MeV [7]. Plot taken from Ref. [30].

Chapter 4

MEASUREMENT OF D(N,NP)N REACTION

The completion of a measurement of the d(n,nd) reaction coupled with new theoretical predictions concerning the neutron-deuteron breakup cross-section (see Figure 8) motivated a study in 2003 to assess the feasibility of measuring the d(n,np)n cross-section [32].

4.1 Feasibility Study (2003)

As mentioned in section 1.2.3, theoretical calculations which included the TM 3NF component [15,33] indicated that the 3NF should make a measurable difference in the d(n,np)n cross-section. Furthermore, the calculations suggested that kinematic regions of the breakup reaction's final-state phase space far from quasi-free kinematics are particularly sensitive to 3NF effects [34]. In the "quasi-free" d(n,np)n reaction the incident neutron can be thought of as scattering from only the neutron or proton in the deuteron. Intuitively, since the 3NF shows up only in the interaction of three particles, it makes sense to look at reactions that are far from this so-called 'quasi-free regime.' An example of a non-quasi free final state would be one nucleon emitted in a far-forward direction and the other at a far backward angle [34, 15].

4.1.1 Detectors

These considerations taken together suggested the experimental setup shown in Figures Figure 27 and Figure 26. Regardless of whether the reaction is quasi-free or not, the d(n,np)n reaction results in two scattered neutrons and a scattered proton. Hence, the detectors and the electronics for data acquisition were set up to detect a neutron and a proton in coincidence. All of this taken together led to two big changes from the setup for elastic scattering in 2001 and 2002. First, because the resulting neutron and proton could be on the same side or opposite sides of the beam line the neutron and proton detectors were laid out in an alternating fashion, symmetric about the beam line. The detectors were located at 8°, 11°, 14°, 17°, 20° and 24° to the left and right of the beam line (see Figure 27). Second, and related to the previous change, the long neutron scintillator bars were replaced with the discrete neutron liquid scintillators used in the 2000 experiment. Unlike the d(n,nd) reaction, outgoing nucleons from the d(n,np)n breakup can be scattered to the same side of the beam line. Hence, the use of the neutron "wall" was inappropriate. The neutron detector at 109.5° on the left-side of the beam line was located at the conjugate angle for np elastic scattering with the CsI charged particle scintillator at 20° on the right side of the beam line. This allowed normalization of the d(n,np)n cross sections to previously collected d(p,pd) data. The ΔE and veto scintillators, visible in Figure 26, were used in the same capacity as in the d(n,nd) experiments, as was the fission chamber.

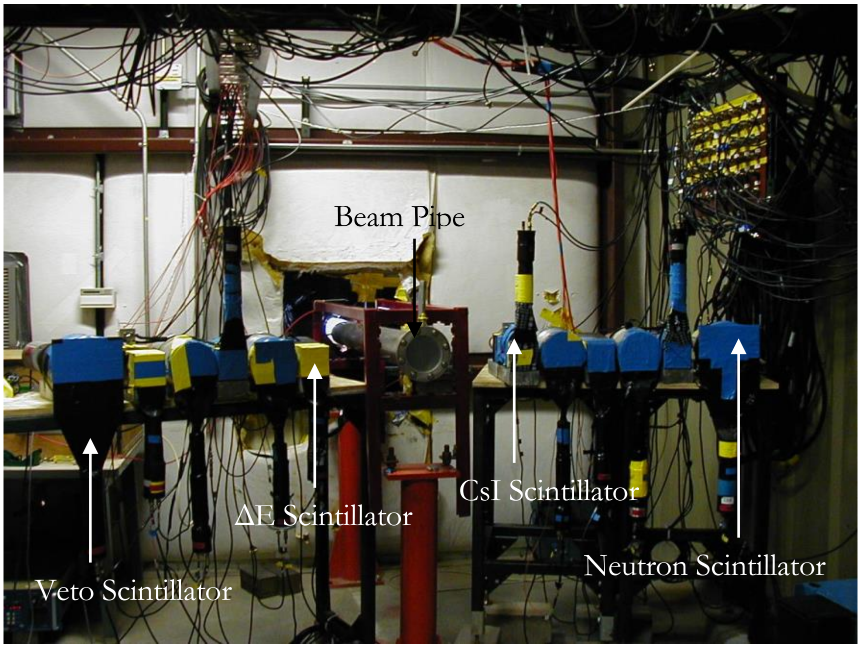

Figure 26. Photograph of the detector layout on flight path 4FP15R at LANSCE (2003). The CsI, organic liquid, veto and ΔE scintillators were located symmetrically about the beam line. The beam pipe which carried residual beam to the beam dump is visible in the center of the photograph.

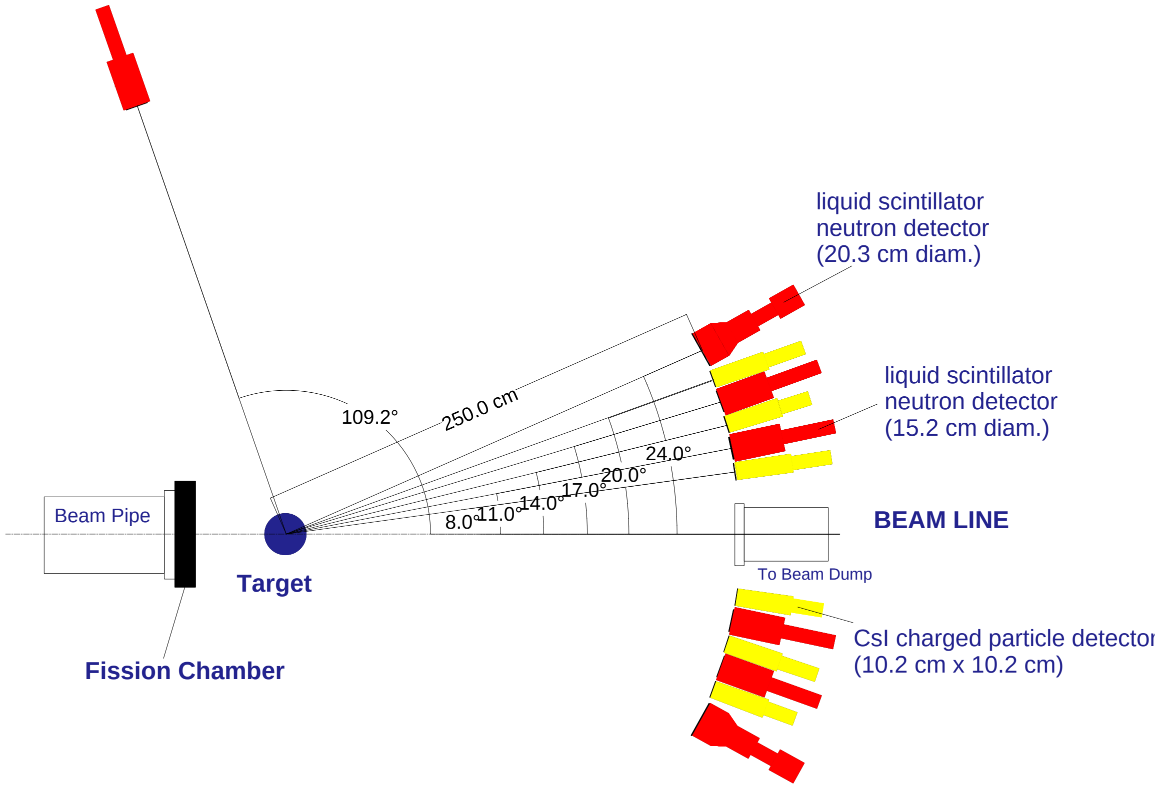

Figure 27. Detector layout for the 2003 feasibility study. The nucleon detectors are arranged symmetrically about the beam line. The proton detectors are CsI crystal scintillators and the neutron detectors are organic liquid scintillators.

4.1.2 Results

Cross section data for d(n,np)n were collected until the middle of October 2003 and then offline analysis began. At around the same time, it was discovered that the 3NF potential on which the theoretical predictions were based did not properly account for chiral symmetry [12,33]. (A system has chiral symmetry if the mirror image of that system is identical in every measurable way.) It is believed that the strong interaction is chirally symmetric (see Ref. [12]). The corrected predictions, using the TM' 3NF component [6] (which does not break chiral symmetry), are quite different, and suggest a different experimental setup.

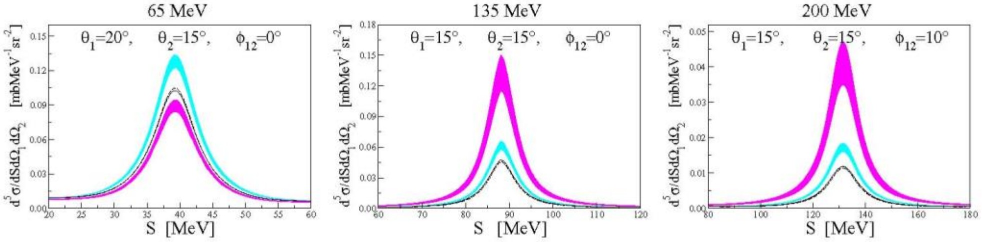

Figure 28. Corrected theory plots for the d(n,np)n cross section, taken from Ref. [33]. The red band is the prediction made with the CD Bonn 2NF [5], the blue band is the prediction made with CD Bonn and the original TM 3NF [12] and the black curve is the prediction made with CD Bonn 2NF and TM' 3NF Ref. [6]. While there is still a difference between the 2NF and TM' 3NF, it is not as large as originally thought.

In addition to the altered theory predictions, it was discovered that the data were corrupted by multiple scattering events, due to the close proximity of the neutron and proton detectors. By placing a thin scintillator detector between adjacent neutron and proton scintillators it was discovered that some protons were scattering from the CsI scintillators into nearby neutron scintillators and thereby triggering both detectors. This is a substantial problem because a neutron-proton coincidence is the signature of a d(n,np)n event and so coincidences are critical to the cross-section measurement.

Table 2 shows the results of measurements that were made to determine the amount of multiple scattering. The target was either empty or filled with liquid hydrogen. The "Wall" row indicates whether beam shielding was in place and where it was located. The "FC*T0" column indicates the number of coincidences between the fission chamber and the T0 beam signal from the accelerator.

Thus, this column indicates the number of incident neutrons. "True P1*N2" is the number of true coincidences between the proton detector labeled P1 and neutron scintillator N2. The numbers for accidental coincidences are listed in the "acc P1*N2" row. To measure the number of accidental coincidences the signal from P1 was delayed so that true coincidences would not register as such with the data acquisition circuitry. Notice that the ratio of true coincidences to accidental events is nearly 1 to 1 for each beam run recorded. Also, notice the high numbers of true coincidences recorded when the target was empty.

Target	LH2	EMPTY	EMPTY	EMPTY	EMPTY
Wall	None/Right	None/Right	Wall/Right	Wall/Right	DoubleWall/Left
FC*T0	188048	187386	183508	168182	175940
true P1*N2	14646	6464	6701	4277	4961
acc P1*N2	11489	4892	5022	2766	3066
true/acc	1.27	1.32	1.33	1.54	1.61

Table 2. True and accidental coincidence rates in several data runs for the 2003 d(n,np)n setup. P1 is the proton detector at 8° on beam left. N2 and NV2 are the neutron detector and veto scintillator at 24° on beam right. Note the near 1 to 1 ratio of true to accidental np coincidences and the high number of true coincidences with an empty target.

It was also discovered that the background count rate on 4FP15R depended upon whether nearby experiments were receiving neutron beams or not. When a nearby experiment had its shutter open, allowing neutrons into the experimental area, the background count rate in the experimental area on 4FP15R would jump. If such a jump were predictable the background could be subtracted in off-line analysis, but this sort of change is effectively random and not accounted for easily.

4.2 Improved Design (2004 – 2005)

The detection array problems discovered in the feasibility study of 2003 as well as the smaller cross section enhancement predictions motivated a much more sophisticated design. Figure 29 is a schematic of the proposed experimental design.

Separating the neutron detectors from the proton detectors was proposed as a solution for minimizing false coincidences due to multiple scattering [35]. It is hoped that by placing a wall of steel and lead shielding next to the left wall of the experimental area and moving the neutron detectors all the way to the back of the experimental area, the problem of unpredictable background due to nearby experiments will be eliminated.

Moving the neutron detectors farther from the target has the added effect of improving the energy resolution for outgoing neutron detection. As mentioned previously, the neutron energy is calculated using time-of-flight information. For the incident neutrons the time of flight from the spallation target to the fission chamber, a distance of 18 m, will be measured. The time from breakup reaction to detection will also be recorded for outgoing neutrons. The neutron detectors themselves will be the same long plastic scintillator bars used in the 2001 – 2002 elastic scattering measurement. However, the new design uses 18 neutron bars mounted with their long axis vertical, 9 on either side of the beam. At a distance of approximately 4 meters from the target, this detection array covers about 14° on either side of the beam providing approximately 1.4° of angular resolution. The resolution for the azimuthal angle φ_{12} is also expected to be around 1.4° [35]. The location of a detected neutron along a neutron scintillator will again be determined using the time difference between signals from the PMTs on the ends of the bars.

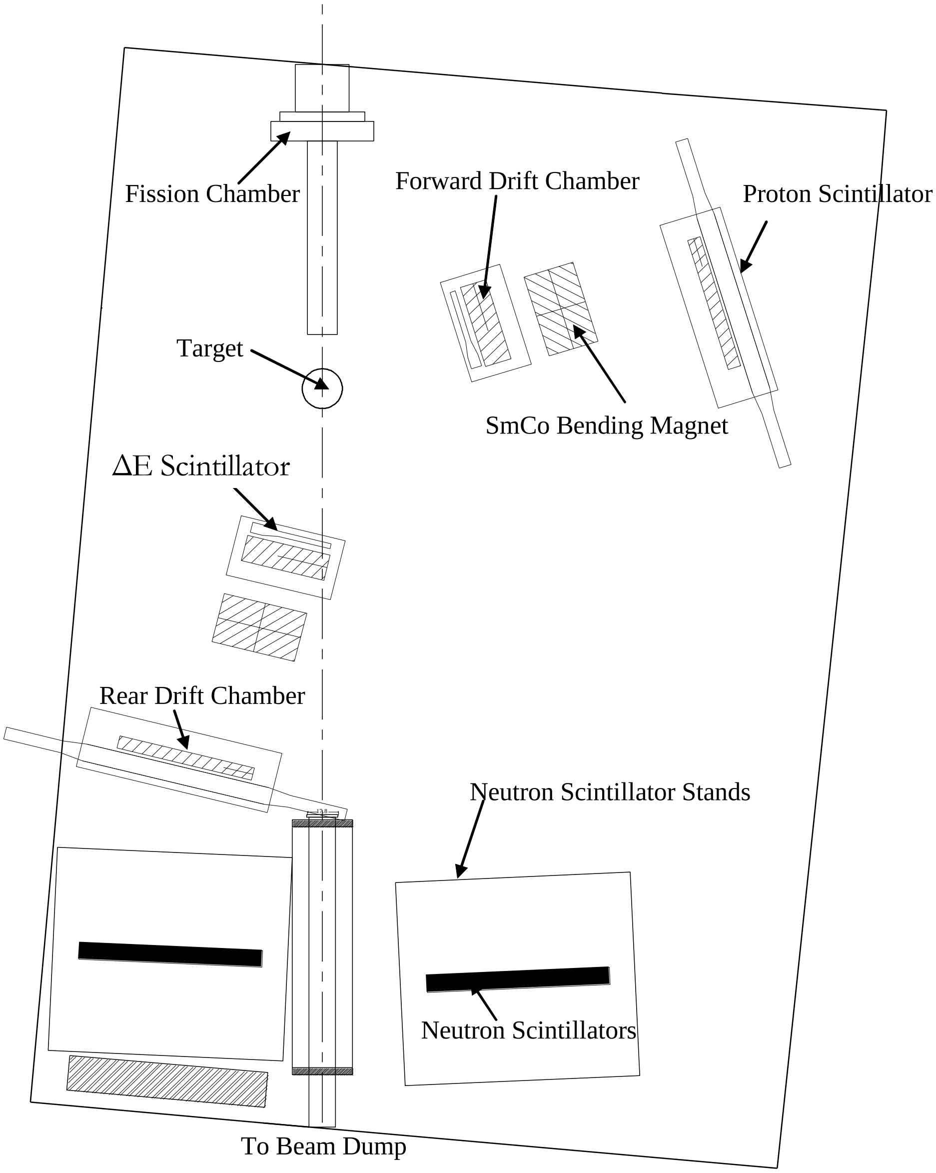

Figure 29. Proposed experimental setup for d(n,np)n reaction measurement in 2005. Notice that the neutron detectors have been moved to the rear of the experimental area. Also, the CsI charged particle scintillation detectors have been replaced by an identical pair of permanent magnet spectrometers. Current plans call for the scintillators at the rear of the spectrometers to be oriented vertically to avoid protruding into the beam.

The plan for proton detection includes a pair of Samarium-Cobalt (SmCo) permanent magnet spectrometers, one deployed around 120° on beam left and the other around 20° on beam right. Each spectrometer employs two sets of drift chambers with a bending magnet in between. Each set of drift chambers consists of two x and y drift chambers about 7 cm apart. The x chamber has an x-plane of horizontal anode wires and the y chamber has a y-plane of vertical anode wires. The anode wires are spaced 8 mm apart in each chamber. Between each pair of anode wires is a cathode wire, as shown in Figure 30. The chambers are sealed with a 6.3 μm mylar foil on each side which is epoxied to the aluminum frames. The chambers will be filled with a mixture of argon and iso-butane gas. As a charged particle travels through a chamber it will ioniz the gas and freed electrons will be drawn to the anode wires which are kept at around -2100 V. The resulting signal will travel to timing to FERA converters (TFC) on each end of the wire. The time difference between signal arrival at each end of the wire will be used to determine which anode wire the particle passed nearest. Also, the sum of the times is related to the time it takes for freed electrons to drift to the anode wires. Hence, knowing the average drift speed, the distance from the particle's path to the nearest anode wire can be determined accurately.

The free electrons will also create a pulse on the nearby "odd" and "even" cathode wires. The pulse is largest on the cathode wire nearest the particle's path. The signals from the "odd" and "even" wires will be bussed into a differential amplifier from which the polarity of the pulse will reveal on which side of the anode wire the particle passed.

The information from the anode and cathode wires, oriented horizontally and vertically, from two adjacent sets of drift chambers will be used to determine a particle's trajectory. After the front set of drift chambers the particle's path will be bent in the magnet's field and then the rear set of drift chambers measures the particle's new trajectory. The radius of curvature of the particle's path will be used to determine its energy and momentum. This proton detection scheme should allow for better proton energy resolution and better angular resolution for proton events. Also, the use of spectrometers should further decrease the occurrence of multiple scattering, as there will be simply less material to scatter from.

At the front of each spectrometer will be a ΔE scintillator, once again for the purpose of distinguishing deuterons from protons. At the rear of each spectrometer is a charged particle scintillator which will be used to start the TFCs.

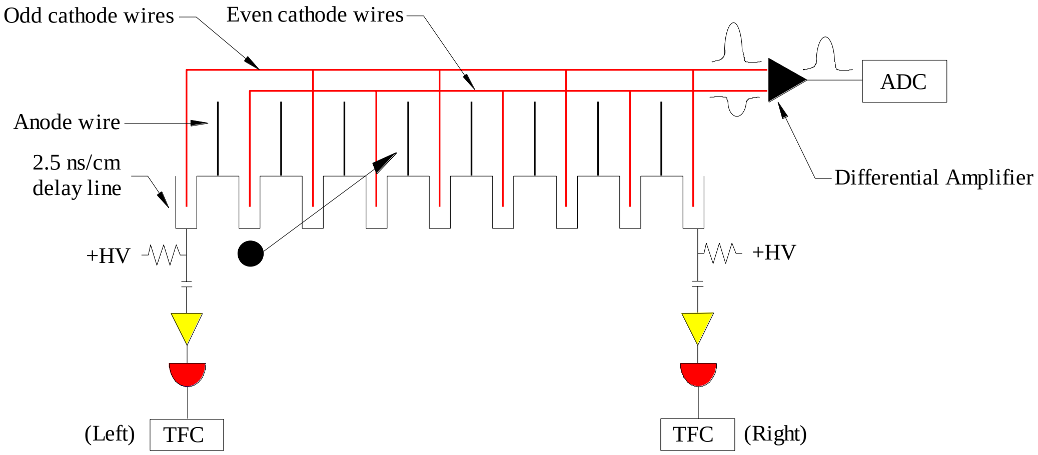

Figure 30 Schematic of a drift chamber circuit taken from Ref. [36]. Charged particles will ionize the gas in the drift chamber. Electrons then drift to the anode wires. The difference in time is determined by which wire the particle was closest to. The sum of the times is related to the distance from the wire. The signals from the cathode wires are used to determine on which side of the anode wire the particle passed.

4.3 Future Plans

The neutron scintillator bars were put in place in the first few months of 2005. During the summer of 2005 it is planned to set up and calibrate the permanent magnet spectrometers and acquisition circuitry for timing. It is also planned to write and update the necessary data acquisition codes for the new detector array. When the LANSCE neutron beam comes online in the fall of 2005 d(n,np)n reaction data will be collected for approximately 40 days. In addition to d(n,np)n measurements, the target will be filled with LH_2 and p(n,np) data will be recorded for the purpose of normalization [33].

Chapter 5

CONCLUSION

QCD is currently our best model for the strong force. Its intrinsic non-linearity, however, makes the prediction of measurable quantities difficult, especially at nuclear energies. This has led to the development of phenomenological models of the strong force. The majority of these models understand the strong force to be a two body interaction, though some include an added 3NF component. The d(n,nd) and d(n,np)n reactions have been examined at LANSCE to study whether the strong force has a three nucleon component. At present, the d(n,nd) cross-section analysis is nearly complete. Initial efforts to measure the d(n,np)n cross section indicated the need for a more sophisticated experimental design. It has been planned to finish the implementation of such a design during the summer of 2005 and measure the d(n,np)n cross section during the fall of 2005.

Appendix A

SCINTILLATOR DETECTORS

This appendix contains general information on scintillation detectors, including the mechanisms by which they function and the advantages of various types.

A.1 Charged Particle Scintillators

For a charged particle, the height of the pulse is proportional to the energy lost by the particle in the scintillator. As the particle passes through the scintillator it interacts, via the Coulomb force, with many of the scintillator's electrons. In each interaction it loses a small amount (on the order of an eV) of energy. The more interactions that occur, the more energy the particle loses and the more light hits the photocathode resulting in a larger pulse. In lieu of a magnetic spectrometer this is a very useful way of determining the energy of charged particles. These experiments have relied primarily on CsI crystal scintillators. When a charged particle enters an inorganic scintillator material it will interact with electrons in the valence band, exciting them to the conduction band. When these excited electrons decay back to the valence band they release a flash of light in the visible range of the EM spectrum. The response time for an inorganic scintillator is on the order of 1 μs.

A.2 Neutron Scintillators

Neutrons themselves will not interact with the electrons in a scintillator, so generally neutron detectors amplify flashes of light that result from nucleon recoil. Thus, the pulse height from a neutron scintillator is not directly related to the detected neutron's energy. An incoming neutron will interact with the nucleus of the scintillator material and some of its energy will be transferred to that nucleus. The recoiling nucleus will then interact with the electrons in the scintillator. Because they rely on nucleon recoil, neutron scintillators are usually composed of a substance with very light nuclei, e.g. Carbon or Hydrogen. For this reason, certain plastics and organic liquids are often used as neutron scintillators.

Generally speaking, light is produced by molecular transitions in an organic scintillator. When a particle interacts with a molecule in an organic scintillator the energy causes the molecule to transition from its ground state to an excited state. The molecule then loses some energy thermally, due to lattice vibrations, before emitting a photon and returning to the ground state configuration. The slight thermal energy loss ensures that the energy required to excite the molecule is different from the energy of the photon emitted in the transition back to the ground state. This energy difference is critical, because otherwise the emission and absorption spectra for the scintillator would be identical and no light would reach the photocathode. The entire process, from excitation to emission, takes on the order of 10^{-8} s and as such, organic scintillators are particularly good for measurements where timing resolution is important.

A.3 Photomultiplier Tube

Figure 31 shows how a scintillation detector works. When a particle enters the scintillating material it releases a flash of light. The detector is normally sealed to prevent light from leaking in or escaping and the walls of the scintillator are silvered and the scintillator is transparent so that the light is not absorbed. This flash of light travels down the light pipe, usually a transparent block of acrylic, and strikes a photocathode. The photocathode is made of a material that releases electrons, via the photoelectric effect, when visible light strikes it. These electrons are released into an evacuated photomultiplier tube (PMT) that contains dynodes connected to a resistor voltage divider. The dynodes are also coated with a substance that will release electrons. Between dynodes the electrons are accelerated through about 100 V and each electron that hits the dynode releases on the order of 3 more. This cascade of electrons results in a negative current running through the final resistor to ground, hence the steep negative voltage pulse. The inherent capacitance of the dynode circuit accounts for the long decay time back to ground. These pulses are then normally amplified and subjected to further processing [19].

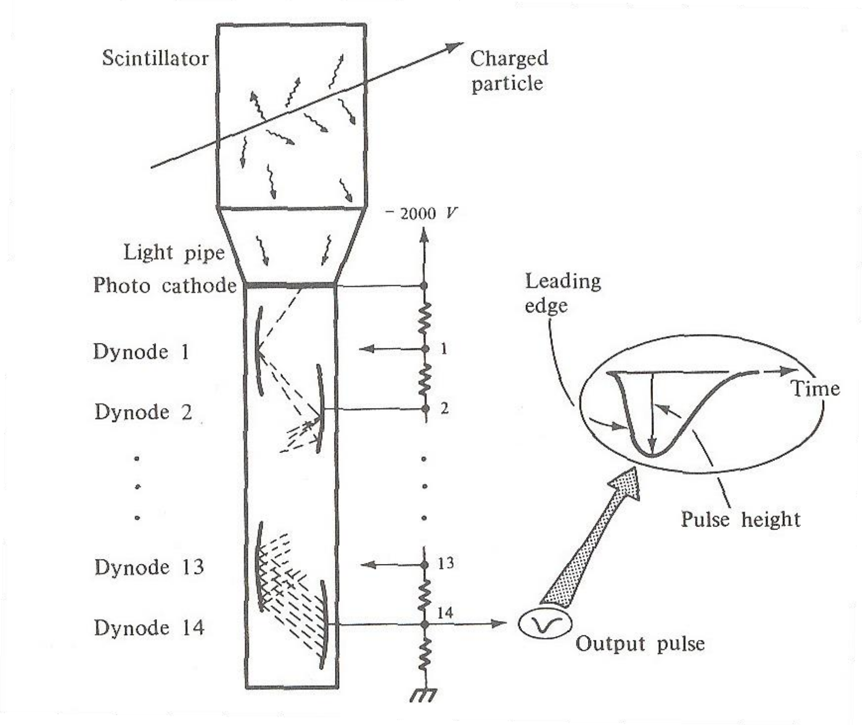

Figure 31. Schematic of a scintillation detector taken from [1]. A charged particle causes the scintillator material to release a flash of light. This light signal is converted to an electrical signal, by the photoelectric effect, at the photocathode and this is amplified and read out by the photomultiplier tube.

Appendix B

CHARGED PARTICLE SPECTROMETERS

The charged particles spectrometers consist of a forward ΔE scintillator, a forward drift chamber, a Samarium-Cobalt (SmCo) permanent bending magnet, a rear drift chamber and a back scintillator. The forward ΔE is used to distinguish deuterons from protons. The pairs of drift chambers, as mentioned in the experimental section, can be used to accurately determine charged particle trajectory. The radius of curvature of the particle's trajectory in the bending magnet can be used to determine the particle's momentum and hence its energy, see Figure 32.

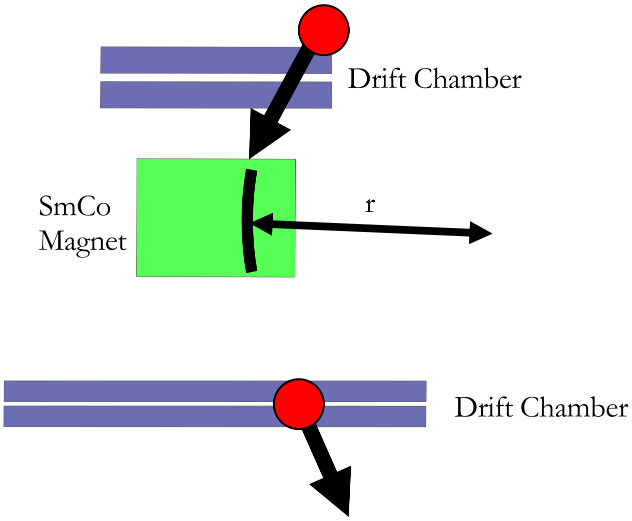

Figure 32. Simplified schematic of a charged particle's trajectory being bent in a constant magnetic field. The first drift chamber is used to determine the particle's trajectory before entering the bending magnet where its path is bent and the resulting trajectory is measured by the rear drift chamber. The radius of curvature in the magnetic field can be used to determine the particle's momentum and energy.

Charged particles experience a force in a magnetic field according to:

$$\vec{F} = q\vec{v} \times \vec{B}\,. \tag{1}$$

If the velocity and the field are orthogonal this simplifies to:

$$F = qvB\ . \tag{2}$$

The magnetic force is a centripetal force, hence:

$$F = \frac{mv^2}{r}\ . \tag{3}$$

Combining equations 2 and 3 and making the substitution p = mv, we have:

$$p = qBr \tag{4}$$

where p is the magnitude of the particle's momentum and r is the radius of curvature of the particle's trajectory in the magnetic field. Though oversimplified, the above derivation does demonstrate how the radius of curvature can be used to determine the momentum and subsequently the energy of a charged particle.

The SmCo magnets that are to be employed in this experiment do not have uniform fields, so to determine the particle's energy, this sort of calculation would be done numerically using a field map of the magnet. This is a non-trivial problem in that the field is not uniform within the magnet and outside of the magnet there are fringe fields. Hence, a calculation of the momentum requires the radius of curvature and vice versa. The momentum of a given particle can be determined by guessing the initial momentum, calculating the change in trajectory in the magnetic field and comparing this with the actual final trajectory of the particle. The difference between the guess and the actual momentum can then be used to make a better guess and this process continues until suitable accuracy is reached.

Appendix C

SCHEMATICS

References

---

[1] H. Frauenfelder and E. M. Henley. *Subatomic Particles*, 2nd ed. (Prentice – Hall, New Jersey, 1991).

[2] V. G. J. Stoks, R. A. M. Klomp, C. P. F. Terheggen and J. J. deSwart, Phys. Rev. **C49**, 2950 (1994).

[3] R. Machleidt, Phys. Rev. **C63**, 024001-1 (2001).

[4] R. B. Wiringa, V. G. J. Stoks, and R. Schiavalla, Phys. Rev. **C51**, 38 (1995).

[5] R. Machleidt, F. Sammarruca, and Y. Song, Phys. Rev. **C53**, R1483 (1996).

[6] S. Nemoto, K. Chmielewski, S. Oryu and P.U. Sauer. Phys. Rev. **C58**, 2599 (1998).

[7] G. Igo *et al.*, Nucl. Phys. **A188**, 33 (1972).

[8] R.E. Adelberger and C.N. Brown, Phys. Rev. **D5**, 2139 (1972).

[9] S. A. Coon and W. Glöckle. Phys. Rev. **C23,** 1790 (1981).

[10] S. A. Coon, M. D. Scadron, P. C. McNamee, B. R. Barrett, D.W.E. Blatt and B.H.J McKellar, Nuclear Physics, **A317,** 242 (1979).

[11] A. Nogga, D. Hüber, H. Kamada and W. Glöckle. Phys. Letters **B409,** 19 (1997).

[12] J. L. Friar, D. Hüber and U. van Kolck. Phys. Rev. **C59,** 53 (1999).

[13] D. Griffiths. *Introduction to Elementary Particles*, 1st ed. (John Wiley and Sons, Inc., New York, 1987).

[14] W. Glöckle, H. Witala, D. Hüber, H. Kamada and J. Golak. Physics Reports **274,** 107 (1996).

[15] J. Kuroś-Żołnierczuk, H. Witala, J. Golak, H. Kamada, A. Nogga, R. Skibinski and W. Glöckle. Phys. Rev. **C66**, 024003 (2002).

[16] *Los Alamos Neutron Science Center Activity Report January – December 2001.* Compiled by A. Archuleta, S. Booth, *et al.* (Los Alamos National Laboratory, NM, 2002), pp. 6 – 9.

[17] Dr. Mark Yuly, April 29, 2005. (private communication).

[18] S. A. Wender, S. Balestrini, *et. al.* Nuclear Instruments and Methods in Physics Research. **A336**, 226 (1993).

[19] Nicholas Tsoulfanidis. *Measurement and Detection of Radiation*, 2nd ed. (Taylor and Francis, Washington, 1995).

[20]J. Matthews, J. Ullman, T. Akdogan, S.A. Wender *et al.* LANSCE Research Proposal #20001531 *Neutron-Deuteron Elastic Scattering and the Three-Nucleon Force,* March 26, 1998. (unpublished).

[21] J. L. Matthews and T. Akdogan. Physica Scripta, **T104**, 49 (2003).

[22] J. L. Matthews, T. Akdogan, M. Chtangeev, *et al.* Research Proposal to the LANSCE PAC. *Neutron-Deuteron Elastic Scattering and the Three-Nucleon Force.* March 29, 2000. (unpublished).

[23] W.R. Leo. *Techniques for Nuclear and Particle Physics Experiments*, 1st ed. (Springer – Verlag, Berlin, 1987).

[24] J. L. Matthews, T. Akdogan, M. Chtangeev, *et al.* Report on Experiment Proposal #20001531 *Neutron-Deuteron Elastic Scattering and the Three-Nucleon Force.* 2001. (unpublished).

[25] J. L. Matthews, T. Akdogan, *et al.* Continuation of Research Proposal #20001531 *Neutron-Deuteron Elastic Scattering and the Three-Nucleon Force.* 2001. (unpublished).

[26] H. Witala, W. Glöckle, D. Hüber, J. Golak and H. Kamada, Physical Review Letters **81**, 1183 (1998).

[27] H. Postma and R. Wilson, Phys. Rev. **121**, 1229 (1961).

[28] H. Sakai, K. Sekiguchi, H. Witala, *et al.*, Phys. Rev. Lett. **84**, 5288 (2000).

[29] K. Ermisch, H.R. Amir-Ahmadi, A.M. van der Berg, *et al.*, Phys. Rev. **C68**, 051001(R) (2003).

[30] Maxim Chtangeev. April 26, 2005. (private communication).

[31] H. Witala, W. Glöckle, D. Hüber, J. Golak and H. Kamada, Physical Review Letters **81**, 1183 (1998).

[32] J. L. Matthews, *Feasibility Study For a Measurement of the Neutron-Induced Deuteron Breakup Cross Section Over a Broad Kinematic Range.* April 28, 2003. (unpublished).

[33] J. L. Matthews, *Investigation of the Neutron-induced Deuteron Breakup Process*, presented to the LANSCE PAC, November 8, 2004 (unpublished).

[34] J. L. Matthews, *et al.* LANSCE Research Proposal #2003525 *Feasibility Study for a Measurement of the Neutron-Induced Deuteron Breakup Cross Section Over a Broad Kinematic Range.* 2003.

[35] Continuation of Research Proposal #2003525 J. Matthews, J. Kuros-Zolnierczuk. *Feasibility Study For a Measurement of the Neutron-Induced Deuteron Breakup Cross Section Over a Broad Kinematic Range.* April 2004.

[36] Rachel DeYoung. Bachelor's Thesis, Houghton College, (2003). (unpublished).